nature COMMUNICATIONS

ARTICLE

https://doi.org/10.1038/s41467-020-16960-9 OPEN

A robust Th-azole framework for highly efficient purification of C_2H_4 from a $C_2H_4/C_2H_2/C_2H_6$ mixture

Zhenzhen Xu[1,5], Xiaohong Xiong[1,5], Jianbo Xiong[1], Rajamani Krishna[2], Libo Li[3], Yaling Fan[1], Feng Luo[1✉] & Banglin Chen[4✉]

Separation of C_2H_4 from $C_2H_4/C_2H_2/C_2H_6$ mixture with high working capacity is still a challenging task. Herein, we deliberately design a Th-metal-organic framework (MOF) for highly efficient separation of C_2H_4 from a binary C_2H_6/C_2H_4 and ternary $C_2H_4/C_2H_2/C_2H_6$ mixture. The synthesized MOF Azole-Th-1 shows a UiO-66-type structure with fcu topology built on a Th_6 secondary building unit and a tetrazole-based linker. Such noticeable structure, is connected by a N,O-donor ligand with high chemical stability. At 100 kPa and 298 K Azole-Th-1 performs excellent separation of C_2H_4 (purity > 99.9%) from not only a binary C_2H_6/C_2H_4 (1:9, v/v) mixture but also a ternary mixture of $C_2H_6/C_2H_2/C_2H_4$ (9:1:90, v/v/v), and the corresponding working capacity can reach up to 1.13 and 1.34 mmol g^{-1}, respectively. The separation mechanism, as unveiled by the density functional theory calculation, is due to a stronger van der Waals interaction between ethane and the MOF skeleton.

---

[1] State key Laboratory of Nuclear Resources and Environment, School of Chemistry, Biology and Material Science, East China University of Technology, 330013 Nanchang, P. R. China. [2] Van't Hoff Institute for Molecular Sciences, University of Amsterdam, Science Park 904, 1098 XH Amsterdam, The Netherlands. [3] College of Chemistry and Chemical Engineering, Shanxi Key Laboratory of Gas Energy Efficient and Clean Utilization, Taiyuan University of Technology, 030024 Taiyuan, Shanxi, China. [4] Department of Chemistry, University of Texas at San Antonio, San Antonio, TX, USA. [5] These authors contributed equally: Zhenzhen Xu, Xiaohong Xiong. ✉email: ecitluofeng@163.com; banglin.chen@utsa.edu

Ethylene is one of the most widely used feedstock molecules for the production of polymers and high-value organic chemicals[1,2]. It is usually produced by the thermal cracking of hydrocarbons. The removal of ethane and acetylene by-products that inevitably arise during these processes is one of the most challenging chemical separations due to the similarity of the physicochemical properties of ethane (kinetic diameter 4.4 Å, boiling point 184.55 K), ethylene (kinetic diameter 4.2 Å, boiling point 169.42 K), and acetylene kinetic diameter 3.3 Å, boiling point 188.40 K)[3–7].

At present, cryogenic distillation is the main technology used to separate ethane and ethylene with the requirement of high pressure (5–28 bar) and low temperature (180–258 K)[8,9], which indicates that this process is expensive and comes with a high energy penalty. And partial hydrogenation of acetylene into ethylene over catalyst[10] or solvent extraction of cracked olefins[11] are also involved with the purification of ethylene from acetylene. Adsorptive separation by porous materials is an alternative technology, especially, some metal-organic frameworks (MOFs)[12–21] with high volume, designable pore characteristics, and countless structural possibilities, can be employed into the gas separation processes, the adsorption selectivity and capacity are higher than the results of conventional adsorbents[22–24] such as zeolites and carbon-based, especially the adsorption and separation for C_2H_6/C_2H_4[8,22,25–39].

For the MOFs with open metal site, the ethylene can easily bind to it, leading to highly selective uptake of ethylene over ethane, due to the electrostatic interaction between the π-electron in ethylene and the positive charge in open metal sites[36,40–44], such as, HKUST-1[44], particularly in the low pressure region, is preferential adsorption of ethylene, which is supported by some theoretical calculations[45,46]. In contract, for some special MOFs, when the coordination positions of metal reaches to saturate, they can enable favorable adsorption towards ethane over ethylene through their unique pore wall that affords stronger van der Waals (vdW) interaction between the H of C_2H_6 and the MOF skeleton[8,22,25–29,32,34,35,47]. For example, ZIF-7 presents the first example of a microporous solid displaying the selective adsorption of paraffins over olefins[48]. However, MOFs showing such uncommon adsorption phenomenon (C_2H_6 over C_2H_4) is still rare until now.

Recently, Lu and co-workers[49] report that they use TJT-100 to obtain the selective adsorption of ethane and acetylene over ethylene from a ternary mixture of $C_2H_2/C_2H_6/C_2H_4$ (0.5:0.5:99, v/v/v) and achieve a C_2H_4 purity greater than 99.9% (working capacity of 0.69 mmol g^{-1}) by a single-breakthrough operation. Zaworoko et al.[38] use a synergistic sorbent separation method for the one-step production of polymer-grade C_2H_4 from ternary ($C_2H_2/C_2H_6/C_2H_4$, working capacity of 0.32 mmol g^{-1}) or quaternary ($CO_2/C_2H_2/C_2H_6/C_2H_4$) gas mixtures with a series of physisorbents. In this regard, constructing MOFs with high working capacity is still highly desirable from the viewpoint of practical application.

The high-valence metal ions are often used to construct stable MOFs, such as Cr(III) for MIL-101[50] and Zr(VI) for UiO-66[51]. However, due to the easy-to-hydrolysis nature of both Cr(III) and Zr(IV), it is still difficult to synthesize Cr(III) and Zr(IV) MOFs with high crystallization. Alternatively, another high-valence metal ion of Th(IV) shows less hydrolytic nature, suggesting an optimal metal ion to generate stable MOFs[52–56]. Generally speaking, according to the hard and soft acid and bases (HSAB) principle, the Zr-based or Th-based MOFs are usually constructed by O-donor carboxylic ligands. For example, the typical UiO-66-type structure is connected by various linear O-donor carboxylic ligands, as shown in the left of Supplementary Fig. 1[51,56,57]. As we know, the N,O-donor ligands such as azole series have been attested to be an excellent organic linkers to construct a great number of MOFs (more than 900 tetrazole-based MOFs and more than 5000 triazole-based MOF from CCDC data)[58–60]. However, there is no Zr-based or Th-based MOFs built on N,O-donor ligands. As shown in the right of Supplementary Fig. 1, the construction of azole-based Zr- or Th-based MOFs is possible, because of the comparable coordination direction for carboxylate and azole molecules, while the introduction of azole unit to bind with Zr or Th ions is also possibly a powerful tool to modulate the electronic structure of metal center and the environment of pore wall, consequently leading to unique physical properties.

In this work, we obtain a successful case via solvothermal reaction of $Th(NO_3)_4$ and 4-(1H-tetrazol-5-yl) benzoic acid (TBA). This compound shows a UiO-66-type structure, except for the replacement of secondary building unit such as Zr_6 by Th_6 and linkers such as O-donor ligand by N,O-donor ligand. This unique tetrazole-based structure allows it to perform high C_2H_6 uptake at room temperature and selective adsorption of C_2H_6 over C_2H_4, finally resulting in the promising application for C_2H_4 separation from the binary C_2H_6/C_2H_4 and ternary $C_2H_4/C_2H_2/C_2H_6$ mixture. Furthermore, both the grand canonical Monte Carlo (GCMC) simulations and density functional theory (DFT) calculations are carried out to disclose the separation mechanism.

Results

Synthesis, structure, and characterization of Azole-Th-1. The reaction between ligand TBA and $Th(NO_3)_4$ in N,N′-dimethylformamide (DMF) yields colorless octahedral crystals of Azole-Th-1 (Supplementary Fig. 2). The synthesis in detail is listed in Supplementary Information. The purity of the bulk samples was confirmed by powder X-ray diffraction (PXRD, Supplementary Fig. 3).

The PXRD discloses that the octahedral crystals of Azole-Th-1 crystallize in the cubic space group *Fm3m*, similar to UiO-66 (Fig. 1c). The length of *a*, *b*, *c* is 23.984(4) Å, longer than UiO-66-Zr (20.743 (5) Å)[51] and UiO-66-Th (21.961(13) Å)[56], mainly due to the longer linker of TBA (ca. 8.4 Å) in Azole-Th-1 than terephthalic acid (ca. 6.8 Å) in UiO-66. Six Th(IV) metal ions are combined together to give the $Th_6O_4(OH)_4(H_2O)_6$ core (Fig. 1b), similar to the $Zr_6O_4(OH)_4(H_2O)_6$ in UiO-66. The Th(IV) ion holds the nine-coordination surrounding with a monocapped square antiprismatic geometry. The Th-O bond length from O^{2-}, OH^-, and H_2O is varied from 2.33 to 2.55 Å, slight shorter than the Th–N bond length of 2.74 Å. As observed in the literature[61,62] for the TBA ligand usually showing highly disordered structure, similar trend is observed in Azole-Th-1 (Supplementary Fig. 4). The TBA ligand contacts with Th(IV) ions via both carboxylate and azole bridge, while two additional nitrogen atoms for each TBA ligand are free-standing without coordination. The 3D framework is formed by both the inorganic $Th_6O_4(OH)_4(H_2O)_6$ core and TBA linkers, where each inorganic core connects to twelve identical $Th_6O_4(OH)_4(H_2O)_6$ cores via twelve TBA linkers, finally constructing the UiO-66-like structure. Similarly, two different types of cages, *viz.* a super tetrahedron cage (Fig. 1d) and a super octahedron (Fig. 1e) with the largest cavity diameter of 1.1 nm and 1.2 nm, respectively, is observed in Azole-Th-1. This is larger the corresponding values of 0.88 nm in UiO-66[51], due to the longer linkers of TBA in Azole-Th-1 than terephthalic acid in UiO-66. The solvent-accessible volume estimated by Platon program[63] is 50.1% of the unit cell, suggesting high porosity of this MOF.

The loss of trapped solvent molecules from Azole-Th-1, according to the thermogravimetric (TG) analysis, is before 75 °C (Supplementary Fig. 5). While the temperature increased to

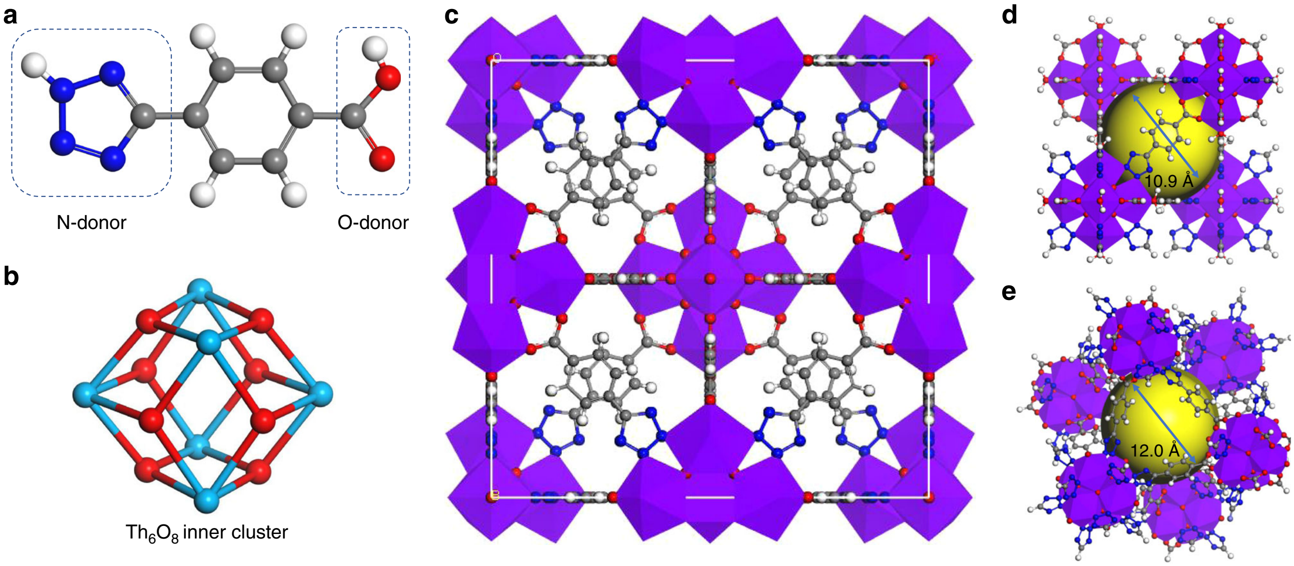

Fig. 1 Main structures. a Ligand TBA, including carboxylic acid donor (O-donor) and tetrazole donor (N-donor), **b** inner core Th_6-cluster drawn alone for clarity (Th_6O_8), **c** unit cell structure in crystal Azole-Th-1, **d**, **e** two types of cages, including super tetrahedron cage **d** and super octahedron cage **e**. Where, Th-light blue ball **b** and polyhedron style **c**–**e** with purple color, O-red ball, C-gray ball, N-blue ball, and H-white ball.

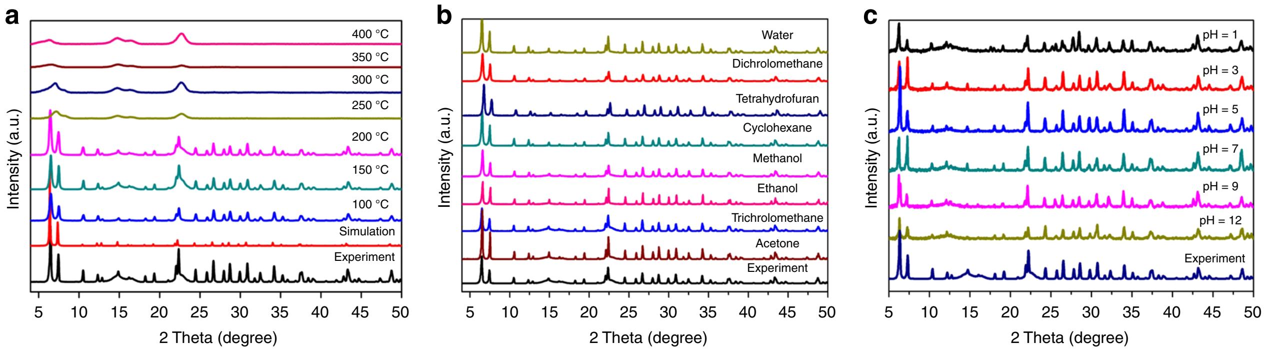

Fig. 2 The PXRD patterns of Azole-Th-1 samples. a Thermal stability from 100 to 400 °C, including simulated and experimental results, **b** soaking in water and seven different organic solvents 30 days, and **c** soaking in different pH solvents 30 days. Source data are provided as a Source Data file.

about 250 °C, the crystal structure begins to collapse, which is in agreement with the results of temperature dependent PXRD tests (Fig. 2a). As shown in Fig. 2a, the PXRD of Azole-Th-1 samples from room temperature to 200 °C are matching with the experimental and simulated results. While the temperature reaches to 250 °C, the peaks of PXRD disappear, which indicates that the crystal structure is destroyed by such high temperature. On the other hand, the chemical stability under water and different solvents environment, including seven organic solvents and a broad pH range from 1 to 12, were also traced by PXRD tests (Fig. 2b, c), where respective optical images of crystal were represented in Fig. 3. Note that the crystals of Azole-Th-1 render excellent stability in water and above solvents even after 30 days.

Adsorption isotherm, selectivity, and breakthrough. The moderate thermal stability and high chemical stability of Azole-Th-1 prompts us to study the gas adsorption performances. To characterize the permanent porosity of the obtained material, the N_2 adsorption isotherm at 77 K was measured. As shown in Fig. 4a, a fully reversible type I isotherm with a Brunauer Emmett Teller (BET) surface area of 983 $m^2\,g^{-1}$ and a uniform pore size around 9.2 Å was exhibited. This pore size is comparable with that calculated LCD (the largest cavity diameter, 10.0 Å) by Zeo++ program[64] (Supplementary Table 3).

This high porosity and desirable aperture encouraged us to further investigate C_2H_6/C_2H_4 separations in detail. Adsorption isotherms of single component C_2H_6 and C_2H_4 were collected at 298 K and 273 K, respectively, as presented in Fig. 4b and Supplementary Fig. 6. The adsorption isotherm of C_2H_6 is typically type I with a steep slope, which is a typical feature of strong adsorbates in microporous materials (Fig. 4b)[8,22,25,27–30,32–35]. And the adsorption amounts of C_2H_6 at both 273 and 298 K (121.7 and 100.2 $cm^3\,g^{-1}$) were also higher than the corresponding C_2H_4 (111.3 and 80.7 $cm^3\,g^{-1}$). Therefore, the Azole-Th-1 has a distinct preference for adsorbing ethane over ethylene. It is well-known that the magnitude of the adsorption enthalpies of porous materials reveals that the affinity of the pore surface toward adsorbents, determining the adsorptive selectivity[39,65]. This can be directly reflected on the adsorption heat enthalpy (Q_{st}) of C_2H_6 and C_2H_4, giving 28.6 kJ mol^{-1} for C_2H_6 at the zero coverage, significantly higher than the values of 26.1 kJ mol^{-1} for C_2H_4 (Fig. 4d), strongly suggesting a higher affinity between host and guest for C_2H_6 than C_2H_4, where the detail virial-type analysis were provided in Supplementary Fig. 7.

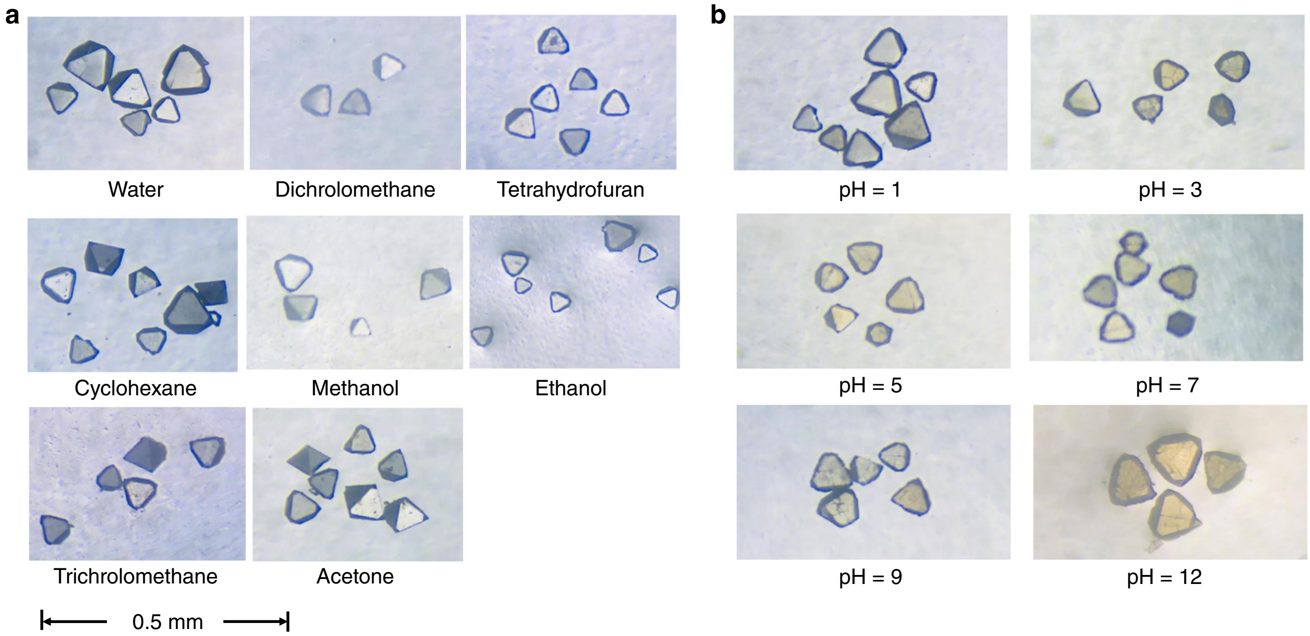

Fig. 3 The optical microscope images of Azole-Th-1 samples. **a** after soaking in water and seven different organic solvents 30 days, **b** after soaking in different pH solvents 30 days.

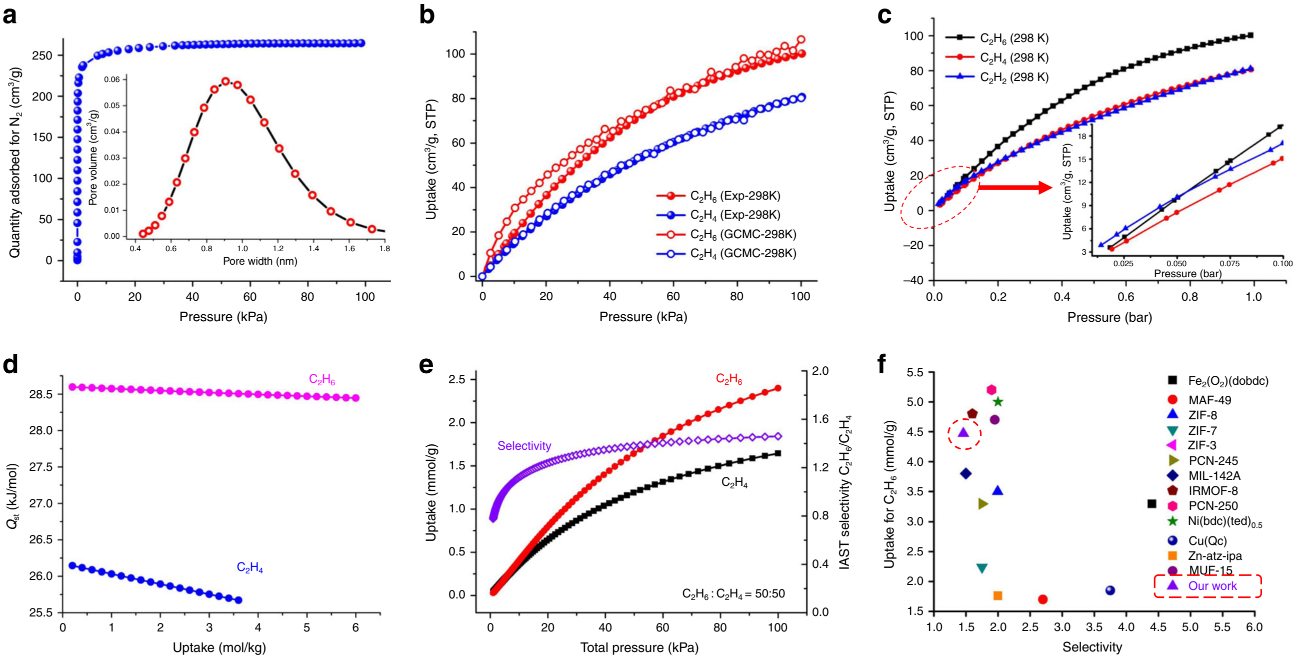

Fig. 4 The adsorption and separation data of Azole-Th-1. **a** The N_2 adsorption at 77 K with the insert of the distribution of pore size. **b** The adsorption isotherms of C_2H_6 and C_2H_4 at 298 K, including experiments and simulations. **c** Experimental adsorption isotherms of Azole-Th-1 for C_2H_6, C_2H_4, and C_2H_2 at 298 K from 0.01 to 1 bar with the insert of enlargement from 0.01 to 0.1 bar. **d** The adsorption heat enthalpy of C_2H_6 and C_2H_4, calculated from the single-component C_2H_6 and C_2H_4 adsorption data at 298 and 273 K. **e** Predicted mixture adsorption isotherms and selectivity of Azole-Th-1 by IAST method for a 50/50 C_2H_6/C_2H_4 mixture at 298 K. **f** A comparison in selectivity and C_2H_6 adsorption capacity at 298 K and 1 bar between the reported top-performing porous adsorbents for C_2H_6/C_2H_4 separation and our MOF. The purple triangle is our MOF. Source data are provided as a Source Data file.

At room temperature and 100 kPa, Azole-Th-1 affords ultrahigh adsorption capacity of C_2H_6 up to 100.2 $cm^3\ g^{-1}$. This value exceeds most reported top-performing porous adsorbents for such use as shown in Table S2, including in $Fe_2(O_2)$(dobdc)[35], MAF-49[22], ZIF-8[34], ZIF-7[32], PCN-245[26], MIL-142A[28], Cu $(Qc)_2$[37], Zn-atz-ipa[38], etc., which are summarized in Fig. 4f. Correspondingly, adsorption capacity of C_2H_4 at the same conditions is 81.1 $cm^3\ g^{-1}$, obviously, less than C_2H_6 about 20 $cm^3\ g^{-1}$. Hence, selective adsorption of C_2H_6 over C_2H_4 is suggested. To estimate the adsorption selectivity, we employed the ideal adsorption solution theory (IAST)[66] to analyze the experimental isotherm data, using composition of 50:50/10:90/1:15 C_2H_6/C_2H_4, as shown in Fig. 4e and Supplementary Fig. 8. The selectivity of C_2H_6 over C_2H_4 was up to 1.46 at room

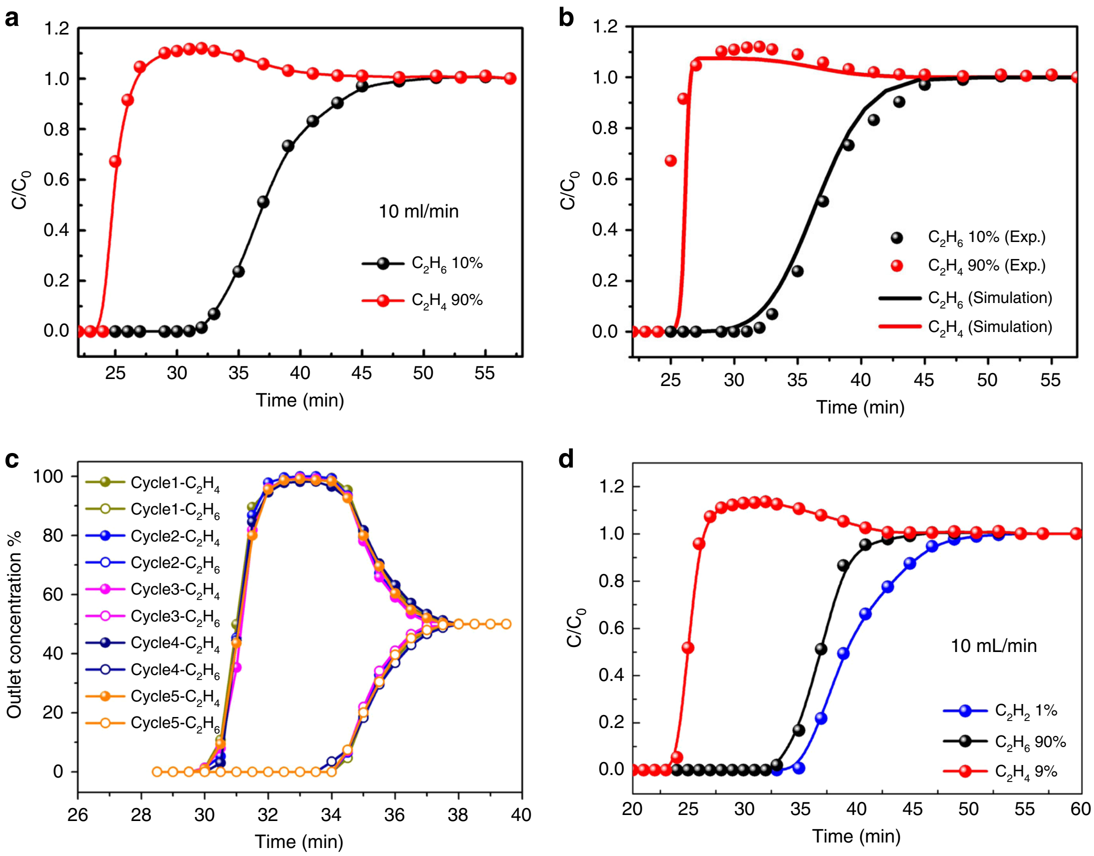

Fig. 5 Experimental breakthrough curves at 298 K and 1 bar on Azole-Th-1. a, **b** C_2H_6/C_2H_4 (10/90, v/v) binary mixture. **c** C_2H_6/C_2H_4 (50/50, v/v) binary mixture for five cycles. **d** $C_2H_6/C_2H_4/C_2H_2$(90/9/1, v/v/v) ternary mixture separation. Source data are provided as a Source Data file.

temperature and 100 kPa, which is slightly higher than that of other ratio mixture, both 1.44 for 10:90 and 1:15 C_2H_6/C_2H_4. To the best of our knowledge, Azole-Th-1 should be the first Th-MOF showing such abnormal adsorption behavior (C_2H_6 over C_2H_4).

Then, in order to check the actual separation ability of the gases mixture, the transient breakthrough simulations for C_2H_6/C_2H_4 (50/50, v/v) mixtures on Azole-Th-1 material was carried out at 298 K, as shown in Supplementary Fig. 9. This result demonstrates that the potential of producing pure product gas C_2H_4 during the time interval $\Delta\tau$, also suggests excellent C_2H_6/C_2H_4 separation performance. And then, to further confirm the real practical separation ability, the actual dynamic adsorption breakthrough experiments for C_2H_6/C_2H_4 (10/90, 50/50, 1/15, v/v) binary mixtures on Azole-Th-1 material were also carried out (Fig. 5a, b, and Supplementary Fig. 10). The C_2H_4 broke through the adsorption bed and yield a high purity gas (>99.9%) at first, whereas after a certain time C_2H_6 slowly eluted and reached to the equilibrium (Fig. 5a, b, and Supplementary Fig. 10). During this period of time, polymer-grade (>99.9%) C_2H_4 can be generated at the outlet. The breakthrough time of ethane was later than that of ethylene for these three ratio mixtures, meaning that the Azole-Th-1 preferred to adsorb ethane over ethylene. The long breakthrough time interval between C_2H_4 and C_2H_6 suggests that the Azole-Th-1 is quite effective for C_2H_6/C_2H_4 separation. The experimental breakthrough results was well in consistent with the simulated breakthrough (Fig. 5b, Supplementary Fig. 10b, d), strongly suggesting its superior application for C_2H_4 purification. Furthermore, cycling breakthrough experiments on Azole-Th-1 were carried out under the same conditions. The breakthrough time interval for C_2H_6/C_2H_4 mixtures in five cycles (Fig. 5c) is comparable, showing that this material has a good regenerability. According to the polymer grade C_2H_4 produced during time interval at different C_2H_4/C_2H_6 ratio, 3 min (50/50), 5 min (90/10), and 3.5 min (15/1), the productivities of C_2H_4 (>99.9%) were 0.68, 1.13, and 0.79 mmol g^{-1}, respectively. Hence, the polymer grade C_2H_4 with the max working capacity of 1.13 mmol g^{-1} with >99.9% purity was harvested from 90/10 gas mixture, which working capacity is nearly 1.3 times for $Fe_2(O_2)$(dobdc) (0.79 mmol g^{-1})[35] and 3.6 times for MAF-49 (0.28 mmol g^{-1})[22], the two best materials for C_2H_6/C_2H_4 separation. Some more detailed comparison with other MOF materials is shown in Supplementary Table 2. After the breakthrough experiments, the PXRD pattern of our sample was also consistent with the PXRD before the breakthrough (Supplementary Fig. 11), which further indicated that this material has a good regenerability and high stability.

Mechanism of gas adsorption by theoretical calculations. Theoretically, the determination of gas adsorption sites in the MOFs is of great significance for the design of some gas storage and separation materials based on MOFs[31,67]. Herein, the ultra-high C_2H_6 storage capacity prompts us to explore the adsorption sites within this Azole-Th-1. Theoretical simulation is a powerful tool enabling us to unveil the adsorption mechanisms and provide the adsorption sites. Therefore, the C_2H_6/C_2H_4 binding affinity in Azole-Th-1 was firstly investigated by single-component sorption isotherms at 298 K and pressures up to 100 kPa. The GCMC simulations were performed for understanding the interactions and adsorption behaviors of C_2H_6 and C_2H_4 in Azole-Th-1 at the molecular level[25,26,33,34,39]. As shown in isotherm of C_2H_6/C_2H_4

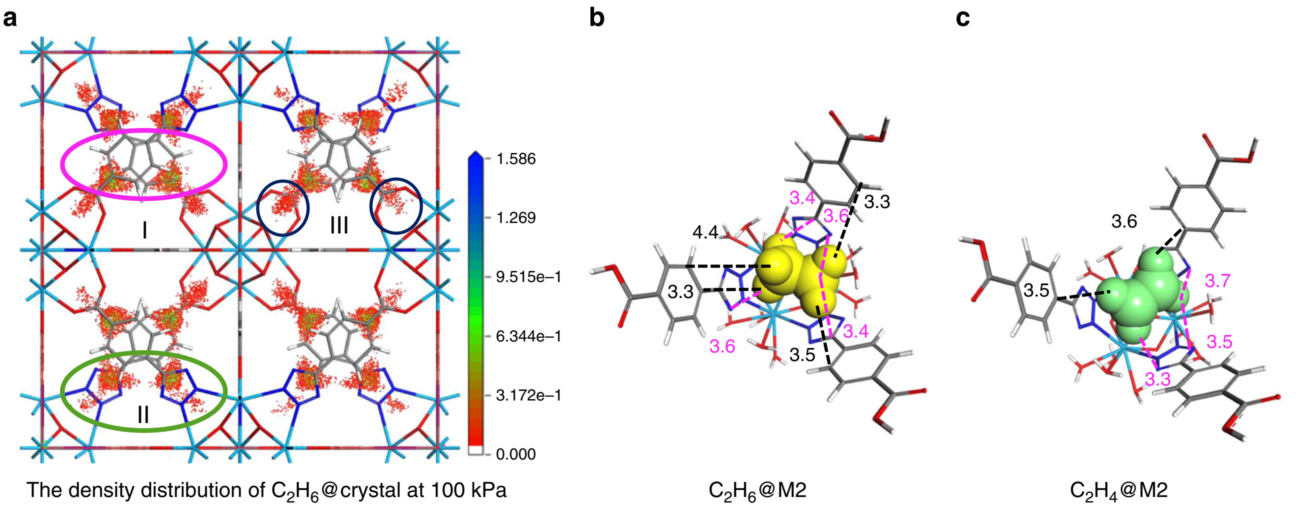

The density distribution of C_2H_6@crystal at 100 kPa

C_2H_6@M2

C_2H_4@M2

Fig. 6 GCMC adsorption simulation and adsorbed structures. **a** The density distribution of C_2H_6 on Azole-Th-1 at 100 kPa and 298 K. **b**, **c** The structures of adsorptions for C_2H_6 and C_2H_4 at M2 model. Where, Th-light blue, O-red, C-gray, N-blue, H-white, C_2H_6-yellow molecule, and C_2H_4-green molecule, and the unit of distance is Å.

adsorption (Fig. 4b), the maximum C_2H_6 and C_2H_4 uptake for Azole-Th-1 are 106.6 and 80.2 $cm^3 g^{-1}$ at 100 kPa and 298 K, respectively, both adsorbed tendency and the adsorption quantity are consistent with the experimental results (100.2 and 80.7 $cm^3 g^{-1}$), where the simulated details are listed in Supplementary Information.

The further investigations on the interaction between C_2H_6/C_2H_4 and MOF material can help us to understand the mechanism of gas adsorption, which could analysis the discrepancies the interactions between C_2H_6 and C_2H_4 with our material, respectively. According to the density distribution of C_2H_6 on Azole-Th-1 at 298 K and 100 kPa (Fig. 6), there are three main adsorbed areas in our material, including benzene region (I-region), the tetrazol heterocycle region (II-region), and carboxylate region (III-region), respectively. Then, the adsorptions under different pressure were analyzed (Supplementary Fig. 12). Due to the higher polarizability of C_2H_6 (44.7×10^{-25} cm^3) compared with C_2H_4 (42.5×10^{-25} cm^3)[7], at the beginning of the adsorption, the C_2H_6 molecules are preferentially filled in region I at 2.6 kPa (Supplementary Fig. 12a), but the C_2H_4 molecules are almost not adsorbed until 10.3 kPa (Supplementary Fig. 12e). While the pressure is 5.1 kPa, the region II begins to be filled by C_2H_6 molecules (Supplementary Fig. 12b), the total capacity of adsorption reaches to 18.5 $cm^3 g^{-1}$, which corresponds to the adsorption capacity of C_2H_4 at 12.8 kPa (18.9 $cm^3 g^{-1}$), at that moment the region II is empty until the pressure increases to 17.9 kPa (Supplementary Fig. 12f). With the increase of pressure (to 48.7 kPa), region I and region II are almost filled saturated by C_2H_6 molecules (Supplementary Fig. 12c), and region III begins to be filled by C_2H_6 already, the total capacity of adsorption reaches to 73.2 $cm^3 g^{-1}$. The vdW interactions between C_2H_6 with aromatic rings (regions I and II) and carboxylate (region III) are more remarkable than the interactions between C_2H_4 with them. While the pressure reaches to 100 kPa, these three regions are saturated generally by C_2H_6 (Supplementary Fig. 12d), whereas, the C_2H_4 molecules only continue to be filled into regions I and II (Supplementary Fig. 12g), the C_2H_6 uptake (106.2 $cm^3 g^{-1}$) is significantly greater than the maximum C_2H_4 uptake (80.2 $cm^3 g^{-1}$). Hence, according to the GCMC simulations, the Azole-Th-1 prefers to adsorbing the C_2H_6 from 0.001 to 100 kPa at 298 K, and the C_2H_6 adsorption capacity is far greater than C_2H_4, which could achieve the separation of C_2H_6 and C_2H_4.

And then, according to the obtained adsorption regions, some DFT theoretical calculations about the mechanism of selective C_2H_6/C_2H_4 in Azole-Th-1 were investigated by the Dmol^3 program package[68] in the MS, the detail calculations were also presented in Supplementary Information. The determination of the adsorption point can quantify the interaction between the gas C_2H_6/C_2H_4 and Azole-Th-1 and analyze the mechanism of the gas adsorption. Because the calculations using the whole unit cell is too large, we used the fragmented cluster models cleaved from the unit cell for modeling the structures and energies to investigate the interaction points of C_2H_6/C_2H_4 adsorption. Due to the highly disordered structure of TBA, four fragment models were constructed. Accordingly, the fragment M1 to M4 were intercepted (Supplementary Fig. 13). Based on the distribution of density of C_2H_6/C_2H_4 through GCMC simulations, the geometries of fragmented models bound to C_2H_6/C_2H_4 were also obtained, as shown in Supplementary Fig. 14. By the calculations of binding energy for adsorbed geometries (Supplementary Table 5), obviously, the interactions between M1 to M4 with C_2H_6 (-43.09 kJ mol^{-1}) were stronger than the interactions between that of fragmented models with C_2H_4 (-33.52 kJ mol^{-1}), which results were in agreement with the heat of adsorption Q_{st}. These can be attributed to the vdW interaction between the C–H in C_2H_6/C_2H_4 and conjugated π-systems in Azole-Th-1, especially, the conjugated region II (tetrazol).

In our opinion, there are three factors for the stabilities of adsorbed structures, the number of H atoms, the distances of vdW interaction, and the polarizability, where the summary about previous two factors were listed in Supplementary Tab. 6. As shown in Supplementary Fig. 14, C_2H_6 and C_2H_4 molecules are bound to several aromatic rings of ligands at three directions within a pore through vdW interactions. A single C_2H_6 or C_2H_4 molecule can form six or four pairs of C–H—π interactions with conjugated regions at least, where the vdW interaction between C–H and benzene ring of ligand (region I) are in the majority. The greater the number of H atoms, the stronger the C–H—π interaction between gas with different models, and finally the greater the adsorption capacity of C_2H_6 compared with C_2H_4.

Because of the use of previously unreported ligand, the conjugated region tetrazole can enhance the binding with gas. As shown in Supplementary Fig. 14, C_2H_6@M1 (all O-donors of ligands coordinated on the Th(IV) inner cluster), there are two pairs of vdW interactions between C–H with carboxylic acid (region III). However, as to C_2H_6@M2 (Fig. 6, all N-donor of ligands coordinated on the Th(IV) inner cluster), because the gas molecule was near to the region II, which contributed to the increasing of the interaction probability between gas and tetrazol. The four pairs of C–H—π interactions with region II could make the adsorption structure more stable with −46.90 kJ mol^{-1} binding energy than the structure without the interaction between C_2H_6 with tetrazol (C_2H_6@M1, −25.87 kJ mol^{-1}).

And then, the average distances between C_2H_6 with benzene region (I), tetrazol region (II), and carboxylic acid region (III) are 3.67, 3.65, and 3.08 Å, respectively. And the average distances between C_2H_4 with these three regions are 3.41 and 3.25 Å (no interaction with region III), which results agreed with the GCMC results (Supplementary Fig. 12g, C_2H_4 only filled into regions I and II). According to these distances of interaction, it is hard to analysis the stabilization of the adsorption structures. Besides the distance and number of C–H—π interactions, C_2H_6 as a more polarizable molecule can interact more strongly by induced dipole interactions with the framework compared to the less polarizable C_2H_4 molecule.

Separation of ternary mixture of $C_2H_6/C_2H_2/C_2H_4$. In traditional C_2H_4 production process, trace amounts of C_2H_2 (about 1%) also exist in the ethylene feed. So, this material was further investigated for the simultaneous capture of C_2H_2 and C_2H_6 from a ternary mixture of $C_2H_6/C_2H_2/C_2H_4$. As shown in Fig. 5d, highly efficient separation of C_2H_4 from a 90:1:9 (v/v/v) gas mixture of $C_2H_6/C_2H_2/C_2H_4$ was achieved by passing the mixture over a packed column of activated Azole-Th-1 material. It can be observed that C_2H_4 achieves a breakthrough first, with no evidence of C_2H_2 or C_2H_6 flow before its breakthrough, which indicates that this material can produce an high purity C_2H_4 (>99.9%) after only a single-breakthrough operation. The working capacity is up to 1.34 mmol g^{-1}, far exceeding the top-performing materials reported by Lu et al. (0.69 mmol g^{-1})[49] and Zaworoko et al. (0.32 mmol g^{-1})[38], strongly suggesting its promising applications in this target. Note that, according to the adsorption isotherm of C_2H_2 (Fig. 4c), the maximum of capacities of C_2H_2 (81.1 cm^3 g^{-1}) and C_2H_4 (80.7 cm^3 g^{-1}) are almost equal to each other. In addition, the adsorption heat enthalpy of C_2H_2 is 25.4 kJ mol^{-1} at the zero coverage, which is lower slightly than Q_{st} of C_2H_4 (26.1 kJ mol^{-1}). And why the high purity of C_2H_4 (>99.9%) can be acquired. Therefore, in order to explore this problem, the C_2H_6, C_2H_4, and C_2H_2 at low pressure region (<0.1 bar) was checked (inserted into Fig. 4c). Before pressure of 0.05 bar, the adsorption of C_2H_2 is obviously bigger than both C_2H_6 and C_2H_4, giving a hierarchy of C_2H_2>C_2H_6>C_2H_4. This is well consistent with the separation conditions of 90:1:9 (v/v/v) gas mixture of $C_2H_6/C_2H_2/C_2H_4$.

Discussion

In a word, we reported a Th-azole framework (Azole-Th-1) by introducing an previously unreported ligand TBA showing a preferential adsorption of ethane over ethylene. Notably, Azole-Th-1 samples exhibited good stability for soaking in water, various organic solvents, and different pH (1–12) solvents about 30 days, respectively. Moreover, preferential adsorption of ethane over ethylene was confirmed by measuring the adsorption isotherms and breakthrough curves. Azole-Th-1 had relative high ethane and ethylene adsorption capacities, 4.5 and 3.6 mmol g^{-1} at 298 K and 100 kPa, respectively. The adsorption selectivity of binary mixture C_2H_6/C_2H_4(1:1, v/v) was ~1.46 at pressure below 100 kPa and 298 K. Five cycles of ethane adsorption–desorption cycle experiments revealed that Azole-Th-1 had a good regenerability. The polymer grade C_2H_4 with the max working capacities of 1.13 mmol g^{-1} with 99.9% purity was harvested from 10/90 gas mixture. Furthermore, Azole-Th-1 also can purify the C_2H_4 (purity >99.9%) from ternary mixture $C_2H_6/C_2H_2/C_2H_4$ (90:1:9, v/v/v) with working capacities of 1.34 mmol g^{-1}. Some DFT calculations suggested that the greater vdW interaction between ethane and Azole-Th-1 than ethylene and material, −43.09 and −33.52 kJ mol^{-1}, respectively, which were in agreement with the isosteric heat of ethane (28.6 kJ mol^{-1}) and ethylene (26.1 kJ mol^{-1}). In brief, these excellent properties, the perfect pH stability and high C_2H_4 purity (>99.9%) from a ternary 90:1:9 mixture of $C_2H_6/C_2H_2/C_2H_4$, etc., make Azole-Th-1 a promising candidate for efficient separation of ethane/ethylene. It will be much more challenging and difficult to separate more complex gas mixtures. Those small gas molecules such as N_2 and CH_4 will not affect the ternary $C_2H_6/C_2H_2/C_2H_4$ separation very much because of their very weak interactions with the framework, leading to very low uptakes of N_2 and CH_4 at the room temperature. However, some other gas molecules, particularly CO_2, is expected to significantly affect the $C_2H_6/C_2H_2/C_2H_4$ separation, because the uptakes of CO_2 are comparable to these C2 hydrocarbons. Until now, no suitable porous materials have been reported yet for the efficient $C_2H_6/C_2H_2/C_2H_4/CO_2$ separation. Before any porous materials can be realized for this very challenging separation, step-by-step separations by different adsorbents will be necessary to get high purity C2 hydrocarbons.

Methods

The synthesis. A mixture of 4-(1H-Tetrazol-5-yl) benzoic acid (TBA, 0.019 g, 0.10 mmol), $Th(NO_3)_4$ (0.048 g, 0.10 mmol), *N,N′*-dimethylformamide (DMF, 3.0 mL), and ionic liquid of tetramethylguanidine chloride (0.015 mg, 0.1 mmol) were placed in a 20 mL screw-capped glass capped jar, then five drops of concentrated hydrochloric acid were added to the mixture. The mixture was sealed and heated at 110 °C for 3 days. The reaction system was cooled to 30 °C with about 6 °C per min cooling rate. After filtration and washed with excess of *N,N′*-dimethylacetamide (DMA), colorless block crystals were collected as a pure phase (see PXRD in Fig. 2).

Gas-adsorption and breakthrough experiments. The original sample about 100 mg was activated at 60 °C under high vacuum for 12 h in gas adsorption apparatus before the gas adsorption measurement. The BET of the MOFs were investigated by nitrogen adsorption and desorption at 77 K using a Belsorp-max. The single-component isotherms of C_2H_6, C_2H_4, and C_2H_2 were collected at 298 and 273 K on a Belsorp-max. The breakthrough separation apparatus consisted of two fixed-bed stainless steel column. One column was loaded with MOF powder (1.9810 g), while the other reactor was used as a blank control group to stabilize the gas flow. The horizontal reactors were placed in a temperature-controlled environment, maintained at 298 K. The flow rates of all gases mixtures were regulated by mass flow controllers, and the effluent gas stream from the column is monitored by a gas chromatography (TCD-Thermal Conductivity Detector, detection limit 0.1%). Prior to each breakthrough experiment, we regenerated the sample by flushing the adsorption bed with helium gas (100 mL per min) for 30 min at 298 K.

Data availability

The X-ray crystallographic coordinated for structure reported in this study has been deposited at the Cambridge Crystallographic Data Centre (CCDC), under deposition number 1969398. This data can be obtained free of charge from the CCDC via https://www.ccdc.cam.ac.uk/structures/. The source data underlying Figs. 2, 4, and 5 and Supplementary Figs. 5, 6, 8, 9, 10a, 10c, and 11 are provided as a Source Data file. And other data, if not included in the article or Supplementary Information or Source Data, are available from the authors on request.

Received: 12 February 2020; Accepted: 21 May 2020;
Published online: 22 June 2020

References

1. Amghizar, I., Vandewalle, L. A., Van Geem, K. M. & Marin, G. B. New trends in olefin production. *Engineering* **3**, 171–178 (2017).
2. He, Y. B., Rajamani, K. & Chen, B. L. Metal–organic frameworks with potential for energy-efficient adsorptive separation of light hydrocarbons. *Energy Environ. Sci.* **5**, 9107–9120 (2012).

3. Li, B. et al. Introduction of pi-complexation into porous aromatic framework for highly selective adsorption of ethylene over ethane. *J. Am. Chem. Soc.* **136**, 8654–8660 (2018).
4. Liao, P. Q., Zhu, A. X., Zhang, W. X., Zhang, J. P. & Chen, X. M. Self-catalysed aerobic oxidization of organic linker in porous crystal for on-demand regulation of sorption behaviours. *Nat. Commun.* **6**, 6350 (2015).
5. Li, J. R., Sculley, J. & Zhou, H. C. Metal-organic frameworks for separations. *Chem. Rev.* **112**, 869–932 (2012).
6. Lee, C. Y. et al. Kinetic separation of propene and propane in metal-organic frameworks: controlling diffusion rates in plate-shaped crystals via tuning of pore apertures and crystallite aspect ratios. *J. Am. Chem. Soc.* **133**, 5228–5231 (2011).
7. Li, J. R., Kuppler, R. J. & Zhou, H. C. Selective gas adsorption and separation in metal-organic frameworks. *Chem. Soc. Rev.* **38**, 1477–1504 (2009).
8. Qazvini, O. T., Babarao, R., Shi, Z. L., Zhang, Y. B. & Telfer, S. G. A robust ethane-trapping metal-organic framework with a high capacity for ethylene purification. *J. Am. Chem. Soc.* **141**, 5014–5020 (2019).
9. Bux, H., Chmelik, C., Krishna, R. & Caro, J. Ethene/ethane separation by the MOF membrane ZIF-8: molecular correlation of permeation, adsorption, diffusion. *J. Membr. Sci.* **369**, 284–289 (2011).
10. Bos, A. N. R. & Westerterp, K. R. Mechanism and kinetics of the selective hydrogenation of ethyne and ethene. *Chem. Eng. Process.: Process Intensification* **32**, 1–7 (1993).
11. Weissermel, K. & Arpe, H. J. *Industrial Organic Chemistry*, 4th edn. (Wiley, New York, 2003).
12. Jin, J., Zhao, X., Feng, P. Y. & Bu, X. H. A cooperative pillar-template strategy as a generalized synthetic method for flexible homochiral porous frameworks. *Angew. Chem. Int. Ed.* **57**, 3737–3741 (2018).
13. Li, H. et al. Microporous metal-organic framework with dual functionalities for efficient separation of acetylene from light hydrocarbon mixtures. *ACS Sustain. Chem. Eng.* **7**, 4897–4902 (2019).
14. Bao, Z. B. et al. Potential of microporous metal-organic frameworks for separation of hydrocarbon mixtures. *Energy Environ. Sci.* **9**, 3612–3641 (2016).
15. Yang, L. F. et al. A single-molecule propyne trap: highly efficient removal of propyne from propylene with anion-pillared ultramicroporous materials. *Adv. Mater.* **30**, 8 (2018).
16. Huang, Y. L. et al. Tuning the C2/C1 hydrocarbon separation performance in a bioMOF by surface functionalization. *Eur. J. Inorg. Chem.* **2019**, 4205–4210 (2019).
17. Nijem, N. et al. Tuning the gate opening pressure of metal-organic frameworks (MOFs) for the selective separation of hydrocarbons. *J. Am. Chem. Soc.* **134**, 15201–15204 (2012).
18. Jin, G. X., Wang, J., Liu, J. Y., Ma, J. P. & Dong, Y. B. Visual recognition and removal of C_2H_2 from C_2H_4/C_2H_2 mixtures by a Cu-I-MOF. *Inorg. Chem.* **57**, 6218–6221 (2018).
19. Luo, M. B. et al. The MOF+ technique: a significant synergic effect enables high performance chromate removal. *Angew. Chem. Int. Ed.* **56**, 16376–16379 (2017).
20. Fan, C. B. et al. Significant enhancement of C_2H_2/C_2H_4 separation by a photochromic diarylethene unit: a temperature- and light-responsive separation switch. *Angew. Chem. Int. Ed.* **56**, 7900–7906 (2017).
21. Luo, F. et al. UTSA-74: a MOF-74 isomer with two accessible binding sites per metal center for highly selective gas separation. *J. Am. Chem. Soc.* **138**, 5678–5684 (2016).
22. Liao, P. Q., Zhang, W. X., Zhang, J. P. & Chen, X. M. Efficient purification of ethene by an ethane-trapping metal-organic framework. *Nat. Commun.* **6**, 8697 (2015).
23. Narin, G. et al. Light olefins/paraffins separation with 13X zeolite binderless beads. *Sep. Purif. Technol.* **133**, 452–475 (2014).
24. Eldridge, R. B. Olefin/paraffin separation technology: a review. *Ind. Eng. Chem. Res.* **32**, 2208–2212 (1993).
25. Chen, Y. et al. An ethane-trapping MOF PCN-250 for highly selective adsorption of ethane over ethylene. *Chem. Eng. Sci.* **175**, 110–117 (2018).
26. Lv, D. et al. Selective adsorption of ethane over ethylene in PCN-245: Impacts of interpenetrated adsorbent. *ACS Appl. Mater. Interfaces* **10**, 8366–8373 (2018).
27. Pires, J., Pinto M. L. & Saini, V. K. Ethane selective IRMOF-8 and its significance in ethane–ethylene separation by adsorption. *ACS Appl. Mater. Interfaces* **6**, 12093–12099 (2014).
28. Chen, Y. et al. Highly adsorptive separation of ethane/ethylene by an ethane-selective MOF MIL-142A. *Ind. Eng. Chem. Res.* **57**, 4063–4069 (2018).
29. Liang, W. et al. Ethane selective adsorbent Ni(bdc)(ted)$_{0.5}$ with high uptake and its significance in adsorption separation of ethane and ethylene. *Chem. Eng. Sci.* **148**, 275–281 (2016).
30. Böhme, U. et al. Ethene/ethane and propene/propane separation via the olefin and paraffin selective metal–organic framework adsorbents CPO-27 and ZIF-8. *Langmuir* **29**, 8592–8600 (2013).
31. Li, J. R. et al. Porous materials with pre-designed single-molecule traps for CO_2 seletive adsorption. *Nat. Commun.* **4**, 1538 (2013).
32. Chen, D. et al. A combined theoretical and experimental analysis on transient breakthroughs of C_2H_6/C_2H_4 in fixed beds packed with ZIF-7. *Microporous Mesoporous Mater.* **208**, 55–65 (2015).
33. Pillai, R. S., Pinto, M. L., Pires, J., Jorge, M. & Gomes, J. R. B. Understanding gas adsorption selectivity in IRMOF-8 using molecular simulation. *ACS Appl. Mater. Interfaces* **7**, 624–637 (2015).
34. Wu, Y., Chen, H., Liu, D., Qian, Y. & Xia, H. Adsorption and separation of ethane/ethylene on ZIFs with various topologies: Combining GCMC simulation with the ideal adsorbed solution theory (IAST). *Chem. Eng. Sci.* **124**, 144–153 (2015).
35. Li, L. et al. Ethane/ethylene separation in a metal-organic framework with iron peroxo sites. *Science* **362**, 443–446 (2018).
36. Lin, R. B. et al. Molecular sieving of ethylene from ethane using a rigid metal-organic framework. *Nat. Mater.* **17**, 1128–1133 (2018).
37. Lin, R. B. et al. Boosting ethane/ethylene separation within isoreticular ultramicroporous metal-organic frameworks. *J. Am. Chem. Soc.* **140**, 12940–12946 (2018).
38. Chen, K. J. et al. Synergistic sorbent separation for one-step ethylene purification from a four-component mixture. *Science* **366**, 241–246 (2019).
39. Fan, W. et al. Fine-tuning the pore environment of the microporous Cu-MOF for high propylene storage and efficient separation of light hydrocarbons. *ACS Cent. Sci.* **5**, 1261–1268 (2019).
40. Zhang, Y. et al. Highly selective adsorption of ethylene over ethane in a MOF featuring the combination of open metal site and pi-complexation. *Chem. Commun.* **51**, 2714–2717 (2015).
41. Luna-Triguero, A., Vicent-Luna, J. M., Gómez-Álvarez, P. & Calero, S. Olefin/Paraffin separation in open metal site Cu-BTC metal–organic framework. *J. Phys. Chem. C* **121**, 3126–3132 (2017).
42. Bloch, E. D. et al. Hydrocarbon separations in a metal-organic framework with open iron(II) coordination sites. *Science* **335**, 1606–1610 (2012).
43. Martins, V. F. D. et al. Ethane/ethylene separation on a copper benzene-1,3,5-tricarboxylate MOF. *Sep. Purif. Technol.* **149**, 445–456 (2015).
44. Wang, Q. M. et al. Metallo-organic molecular sieve for gas separation and purification. *Microporous Mesoporous Mater.* **55**, 217–230 (2002).
45. Wang, S. Y., Yang, Q. Y. & Zhong, C. L. Adsorption and separation of binary mixtures in a metal-organic framework Cu-BTC: A computational study. *Sep. Purif. Technol.* **60**, 30–35 (2008).
46. Nicholson, T. M. & Bhatia, S. K. Electrostatically mediated specific adsorption of small molecules in metallo-organic frameworks. *J. Phys. Chem. B* **110**, 24834–24836 (2006).
47. Cai, J. et al. A doubly interpenetrated metal–organic framework with open metal sites and suitable pore sizes for highly selective separation of small hydrocarbons at room temperature. *Cryst. Growth Des.* **13**, 2094–2097 (2013).
48. Gücüyener, C., van den Bergh, J., Gascon, J. & Kapteijn, F. Ethane/ethene separation turned on its head: selective ethane adsorption on the metal-organic framework ZIF-7 through a gate-opening mechanism. *J. Am. Chem. Soc.* **132**, 17704–17706 (2010).
49. Hao, H. G. et al. Simultaneous trapping of C_2H_2 and C_2H_6 from a ternary mixture of $C_2H_2/C_2H_4/C_2H_6$ in a robust metal–organic framework for the purification of C_2H_4. *Angew. Chem. Int. Ed.* **57**, 16067–16071 (2018).
50. Férey, G. et al. A chromium terephthalate-based solid with unusually large pore volumes and surface area. *Science* **309**, 2040–2042 (2005).
51. Jasmina Hafizovic, Cavka et al. A new zirconium inorganic building brick forming metal organic frameworks with exceptional stability. *J. Am. Chem. Soc.* **130**, 13850–13851 (2008).
52. Dolgopolova, E. A., Rice, A. M. & Shustova, N. B. Actinide-based MOFs: a middle ground in solution and solid-state structural motifs. *Chem. Commun.* **54**, 6472–6483 (2018).
53. Dolgopolova, E. A. et al. Multifaceted modularity: A key for stepwise building of hierarchical complexity in actinide metal–organic frameworks. *J. Am. Chem. Soc.* **139**, 16852–16861 (2017).
54. Ok, K. M., Sung, J. Y., Hu, G., Jacobs, R. M. J. & O'Hare, D. TOF-2: A large 1D channel thorium organic framework. *J. Am. Chem. Soc.* **130**, 3762–3763 (2008).
55. Wang, Y. et al. Employing an unsaturated Th(4+) site in a porous thorium-organic framework for Kr/Xe uptake and separation. *Angew. Chem. Int. Ed.* **57**, 5783–5787 (2018).
56. Falaise, C., Charles, J. S., Volkringer, C. & Loiseau, T. Thorium terephthalates coordination polymers synthesized in solvothermal DMF/H_2O system. *Inorg. Chem.* **54**, 2235–2242 (2015).
57. Puchberger, M. et al. Can the clusters $Zr_6O_4(OH)_4(OOCR)_{12}$ and $[Zr_6O_4(OH)_4(OOCR)_{12}]_2$ be converted into each other? *Eur. J. Inorg. Chem.* **2006**, 3283–3293 (2006).
58. Burgun, A. et al. Mapping-out catalytic processes in a metal–organic framework with single-crystal X-ray crystallography. *Angew. Chem. Int Ed.* **56**, 8412–8416 (2017).
59. Sun, W. Q. et al. Programmable self-assembly of heterometallic Palladium (II)–Copper(II) 1D grid-chain using dinuclear Palladium(II) corners with pyrazole–carboxylic acid ligands. *Chem. Asian J.* **13**, 1108–1113 (2018).

60. Chen, D. M. et al. Microporous cobalt(II)–organic framework with open O-donor sites for effective C_2H_2 storage and C_2H_2/CO_2 separation at room temperature. *Inorg. Chem.* **56**, 14767–14770 (2017).
61. Wang, D., Zhao, T., Li, G., Huo, Q. & Liu, Y. A porous sodalite-type MOF based on tetrazolcarboxylate ligands and $[Cu_4Cl]^{7+}$ squares with open metal sites for gas sorption. *Dalton Trans.* **43**, 2365–2368 (2014).
62. Pachfule, P., Chen, Y., Sahoo, S. C., Jiang, J. & Banerjee, R. Structural isomerism and effect of fluorination on gas adsorption in copper-tetrazolate based metal organic frameworks. *Chem. Mater.* **23**, 2908–2916 (2011).
63. Spek, A. L. PLATON. Utrecht University (2001).
64. Willems, T. F., Rycroft, C. H., Kazi, M., Meza, J. C. & Haranczyk, M. Algorithms and tools for high-throughput geometry—based analysis of crystalline porous materials. *Microporous Mesoporous Mater.* **149**, 134–141 (2012).
65. Yang, Y. Y., Lin, Z. J., Liu, T. T., Liang, J. & Cao, R. Synthesis structures and physical properties of mixed-ligand coordination polymers based on a V-shaped dicarboxylic ligand. *Cryst. Eng. Commun.* **17**, 1381–1388 (2015).
66. Myers, A. & Prausnitz, J. M. Thermodynamics of mixed gas adsortion. *AIChE J.* **11**, 121–127 (1965).
67. Kubota, Y. et al. Metastable sorption state of a metal-organic porous material determined by in situitu synchrotron powder diffraction. *Angew. Chem. Int. Ed.* **45**, 4932–4936 (2006).
68. Delley, B. From molecules to solids with the $Dmol^3$ approach. *J. Chem. Phys.* **113**, 7756 (2000).

Acknowledgements

We thanks to the National Natural Science Foundations of China (21966002, 21871047, 21661001, and 21922810), the Natural Science Foundation of Jiangxi Province of China (20181ACB20003), and the Training Program for Academic and Technical Leaders of Major Disciplines in Jiangxi Province (20194BCJ22010).

Author contributions

B.C. and F.L. conceived and designed the research, and gave valuable comments on the analysis; L.L. carried out the transient breakthrough experiments; R.K. calculated the selectivity and simulated the breakthrough; Z.X. carried out all theoretical calculations and interpretations, created all figures and wrote the draft; X.X., J.X., and Y.F. carried out experiments.

Competing interests

The authors declare no competing interests.

Additional information

Supplementary information is available for this paper at https://doi.org/10.1038/s41467-020-16960-9.

Correspondence and requests for materials should be addressed to F.L. or B.C.

Peer review information *Nature Communications* thanks Shane Telfer, Michael Zaworotko and the other, anonymous, reviewer(s) for their contribution to the peer review of this work. Peer reviewer reports are available.

Reprints and permission information is available at http://www.nature.com/reprints

Supplementary Information

A robust Th-Azole framework for highly efficient purification of C_2H_4 from a $C_2H_4/C_2H_2/C_2H_6$ mixture

Xu et al.

Supplementary Information include:

Supplementary Method 1 to 8

Supplementary Tables 1 to 6

Supplementary Figures 1 to 14

Supplementary References 1 to 31

Supplementary Methods 1. Materials and Physical Measurements

Caution! Th-232 used in this study is an α emitter with the daughter of radioactive Ra-228. All thorium compounds used and investigated were operated in an authorized laboratory designed for actinide element studies. Standard precautions for handling radioactive materials should be followed. The reagents and solvents were commercially available and were used as received without further purification, where the ligand 4-(1H-Tetrazol-5-yl) benzoic acid ($C_8H_6N_4O_2$, 95%) from EXTENSION Technology Co., Ltd was purchased and directly used, Thorium nitrate hydrate ($N_4O_{12}Th$, Aladdin), Tetramethylguanidine chloride ($C_5H_{14}N_3Cl$, 98%, Aladdin), hydrochloric acid (HCl, Aladdin), and solvents (N, N’-dimethylformamide and N, N’-dimethylacetamide, HPLC grade of 99.9%) from Aladdin Chemistry Co. Ltd were also purchased and directly used.

The optical images were accepted from Optec SZ810 microscope. Thermogravimetric analysis (TG) was performed by a TGA Q600 thermal analysis system. All TG experiments were performed under a N_2 atmosphere from room temperature to 800 °C at a rate of 2°C/min. Data were analyzed using the TA Universal Analysis software package. X-ray powder diffraction were collected by a Bruker AXS D8 Discover powder diffractometer at 40 kV, 40 mA for Cu Kα (λ = 1.5406 Å) at room temperature in the range of 5-50 degree (2 theta) with a scan speed of 0.1 degree per step. The gas sorption isotherms were collected on a Belsorp-max. Ultrahigh-purity-grade (> 99.999%) N_2, C_2H_6, C_2H_4, and C_2H_2 gases were used in this adsorption measurement. To maintain the experimental temperatures, liquid nitrogen (77 K) and a temperature-programmed water bath (273 and 298 K) were used, respectively.

Supplementary Methods 2. Powder X-ray diffraction (PXRD)

For PXRD measurements, the samples were always kept damp with solvent prior to and during measurements. The two-dimensional image of the Debye rings were integrated with 2 Dp to give 2 theta ~ intensity diffractograms. Predicted powder patterns were generated from single crystal structures using Mercury. Powder diffraction patterns, as shown in the following figure revealed that the structure of Azole-Th-1 remains unchanged after soaked in ethanol, acetone, tetrahydrofuran, pure water, methanol cyclohexane, trichrolomethane, and dichrolomethane, respectively (Fig. 2b). The thermal stabilities from 100 to 400℃ were also tested, which results indicated that the structure of Azole-Th-1 began to be destroyed after 20,0 ℃ (Fig. 2a). The PXRD of soaking in the solvents with the range of pH from 1 to 12 were tested (Fig. 2c). Furthermore, the PXRD before and after breakthrough experiments is also compared in Supplementary Fig. 11.

Supplementary Methods 3. Structure, physical properties and pore shape of Azole-Th-1

The Zeo++ code[1, 2]were used to characterize the geometric features of the crystal structure of Azole-Th-1 by calculating the pore volume with the use of N_2 probe molecule, the pore limiting diameter (i.e., the diameter of smallest pore window), the largest cavity diameter (i.e., the diameter of the largest sphere that can fit within the pores), and the surface area accessible to a N_2 probe using the coordinated found by X-ray crystallography. The Accelrys Materials Studio (MS) 8.0 software package[3, 4, 5] was used to visualize the MOF structure and pore topology.

Supplementary Methods 4. Calculation of isosteric heat of adsorption

The binding energy is reflected in the isosteric heat of adsorption, Q_{st}, is calculated from the Clausius-Clapeyron equation, as shown in Supplementary Equation 1,

$$Q_{\mathrm{st}} = -RT^2\left(\frac{\partial \ln p}{\partial T}\right)_q \qquad (1)$$

where p is the pressure, T is the temperature, R is the gas constant (8.314 J $\mathrm{mol^{-1}\ K^{-1}}$). By drawing the ln p vs $1/T$ plot of gas at various loadings, Q_{st} = -slope × R. To extract the coverage-dependent isosteric heat of adsorption, the data were modeled with a virial-type expression[6, 7] composed of parameters a_i and b_i that are independent of temperature:

$$\ln(p) = \ln(N) + \frac{1}{T}\sum_{i=0}^{m} a_i N_i + \sum_{i=0}^{n} b_i N_i \qquad (2)$$

$$Q_{\mathrm{st}} = -R\sum_{i=0}^{m} a_i N_i \qquad (3)$$

where N is the amount adsorbed (or uptake), m and n determine the number of terms required to adequately describe the isotherm. The isosteric heat of adsorption is calculated according to Supplementary Equation 3. The coverage dependencies of Q_{st} calculated from fitting the 273 and 298 K data are presented graphically in Fig. 4d, and the virial equation fit for C_2H_6, C_2H_4, and C_2H_2 adsorption isotherms of Azole-Th-1 are shown in Supplementary Fig. 7.

Supplementary Methods 5. Calculation of selectivity via ideal adsorption solution theory (IAST)

The adsorption selectivity of C_2H_6/C_2H_4 (50/50, 10/90, 1/15, v/v) in Azole-Th-1 was established by using the Ideal Adsorption Solution Theory (IAST). The adsorption selectivity for C_2H_6/C_2H_4 separation is defined by,

$$S_{\mathrm{ads}} = \frac{x_{\mathrm{C_2H_6}}/x_{\mathrm{C_2H_4}}}{y_{\mathrm{C_2H_6}}/y_{\mathrm{C_2H_4}}} \qquad (4)$$

where, $x_{\mathrm{C_2H_6}}$ and $x_{\mathrm{C_2H_4}}$ are the equilibrium adsorption capacity of component C_2H_6 and component C_2H_4, respectively, and $y_{\mathrm{C_2H_6}}$ and $y_{\mathrm{C_2H_4}}$ are the molar fractions of component C_2H_6 and component C_2H_4 in the gas phase.

Fitting details: The adsorption data for C_2H_6, C_2H_4, and C_2H_2 in Azole-Th-1 at 273 K and 298 K were fitted with the single-site Langmuir model,

$$q = q_{\mathrm{sat}} \frac{bp^{\nu}}{1+bp^{\nu}} \qquad (5)$$

with *T*-dependent parameters *b*,

$$b = b_0 \exp\left(\frac{E}{RT}\right) \qquad (6)$$

where the single-site Langmuir parameters for C_2H_6, C_2H_4, and C_2H_2 are provided in Supplementary Tab. 4.

Supplementary Methods 6. Computational calculations

Density Functional Theory calculations: DFT calculations were performed to provide the optimized structures and energies of C_2H_6/C_2H_4 interaction with the frameworks of Azole-Th-1. The Perdew-Burke-Ernzerhof (PBE) function[8, 9] under the generalized gradient approximation (GGA) functional with the double-ξ numerical polarization (DPN) basis set was used by Dmol^3 program package[10] in the MS of Accelrys[3, 4, 5]. Since the calculations using the whole unit cell too large, we used fragmented cluster models cleaved from the unit cells for modeling the partial charges, structures, and energies, the smaller fragmented models were used as presented in Supplementary Fig. 13. The boundaries of models were saturated by H_2O molecules. The tolerances of energy, gradient and displacement convergence were, 2×10^{-4} hartree, 4×10^{-3} hartree Å^{-1}, and 5×10^{-3} Å, respectively. The binding energy (ΔE_{bind}) for C_2H_6/C_2H_4 with models was calculated by Supplementary Equation 7,

$$\Delta E_{\mathrm{bind}} = E_{\mathrm{complex}} - E_{\mathrm{gas}} - E_{\mathrm{MOF(model)}} \qquad (7)$$

where, E_{complex}, E_{gas}, and $E_{\mathrm{MOF\ (model)}}$ are the total energies of complex of gas with model, single C_2H_6/C_2H_4 gas, and MOF model at the optimized geometries, respectively.

Grand Canonical Monte Carlo (GCMC) Simulations: The GCMC simulations, which were performed by Sorption code[4, 11] in MS software[3, 4, 5], were carried out to investigate on the adsorbed capacity of Azole-Th-1 for C_2H_6/C_2H_4 at 298 K from 0.001 to 100 kPa. A simulation box of 1×1×1 crystallographic unit cell was used. During the simulations, 4×10^6 steps were performed to guarantee the equilibration and to sample the desired properties, respectively. Rigid framework assumption was used in all simulations. The Dreiding forcefield parameter[12] was used to describe the interactions, the van der Waals interaction with a cutoff of 15.5 Å were depicted by Lenard-Jones 12-6 potential.

Supplementary Methods 7. Thermogravimetric analysis

Thermogravimetric analysis (TG) was performed by a TGA Q600 thermal analysis system. All TG experiments were performed under a N_2 atmosphere from room temperature to 800 °C at a rate of 2 °C /min.

Supplementary Methods 8. Breakthrough curve simulations

The performance of industrial fixed bed adsorbers is dictated by a combination of adsorption selectivity and uptake capacity. Transient breakthrough simulations were carried out for 50/50, 90/10, and 15/1 binary C_2H_4(1)/C_2H_6(2) mixtures and 9/1/90 ternary C_2H_6/C_2H_2/C_2H_4 mixture in Azole-Th-1 operating at a total pressure of 100 kPa and 298 K, using the methodology described in earlier publications.[13, 14, 15, 16] The numerical details of the code implementation are provided online by Krishna and Baur.[17] For the breakthrough simulations, the following parameter values were used: length of packed bed, L = 0.3 m; voidage of packed bed, ε = 0.4; superficial gas velocity at inlet, u = 0.04 m s^{-1}.

The Supplementary Fig. 9 shows result of the breakthrough calculations. The y-axis is the dimensionless concentrations of each component at the exit of the fixed bed, normalized with respect to the inlet feed concentrations. The *x*-axis is the dimensionless time, $\tau = {}^{tu}/_{L\varepsilon}$, defined by dividing the actual time, *t*, by the characteristic time, ${}^{L\varepsilon}/_{u}$.

Notation

b	Langmuir-Freundlich constant, $\mathrm{Pa}^{-\nu}$
q	component molar loading of species i, mol kg^{-1}
q_{sat}	saturation loading, mol kg^{-1}
L	length of packed bed adsorber, m
t	time, s
T	absolute temperature, K
u	superficial gas velocity in packed bed, m s^{-1}
p	pressure, Pa
R	gas constant, 8.314 J mol^{-1} K^{-1}

Greek letters

ε	voidage of packed bed, dimensionless
ν	Freundlich exponent, dimensionless
τ	time, dimensionless

Supplementary Table 1. Crystal data of disorder Azole-Th-1.

	Azole-Th-1
Formula	$Th_6O_4(OH)_4(H_2O)_6(TBA)_6$
Empirical formula	$C_{24}H_{12}N_{12}O_{13}Th_3$
Formula weight	1372.58
Temperature (K)	293
Wavelength (Å)	0.71073
Crystal system	Cubic
Space group	$Fm\bar{3}m$
Unit cell dimensions (Å)	a=23.9839 b=23.9839 c=23.9839
Cell Volume ($Å^3$)	13796.2
Density	1.322
Theta range for data collection (degree)	3.4-24.97
Crystal parameters(degree)	α=90.000 β=90.000 γ=90.000
Z	8
F(000)	4912
Crystal size (mm)	0.10×0.10×0.08
GOF	1.084
Final R indices [I> 2 sigma (I)]	R1=0.0199 wR1=0.0512
Final R indices [all]	R1=0.0225 wR1=0.0532

Supplementary Table 2. A summary of reported porous adsorbents for C_2H_6/C_2H_4 separation at 1bar and 298 K.

	C_2H_6/C_2H_4 Uptakes (mmol g^{-1})	C_2H_6/C_2H_4 Selectivity (50/50)	Q_{st} (kJ mol^{-1})
$Fe_2(O_2)$(dobdc)[18]	3.3/2.5	4.4	66.8/38
MAF-49[19]	1.70/1.65	2.7	60/48
IRMOF-8[18, 20]	4.8/3.4	1.6	52.5/50.5
ZIF-8[21]	3.5/1.8	1.99	22.2/16.3
ZIF-7[22, 23, 24]	2.24/2.2	1.75	27.3/24.7
ZIF-3[21]	6.0/5.5	2.22	28.5/23.8
PCN-250[25]	5.2/4.1	1.9	23.6/21.1
Ni(bdc)$(ted)_{0.5}$[26]	5/3.2	2.0	21.5/18.3
MUF-15[27]	4.7/4.2	1.95	29.2/28.2
PCN-245[28]	3.3/2.4	1.75	23/20.5
MIL-142A[29]	3.8/2.9	1.5	27.3/26.2
$Cu(Qc)_2$[30]	1.85/0.78	3.75	29/25.4
Zn-atz-ipa[31]	1.76/1.75	2.0	45.8/40
Our MOF	**4.5/3.6**	**1.46**	**28.6/26.1**

Supplementary Table 3. Some calculated and experimentally determined structural characteristics of Azole-Th-1.

	Azole-Th-1
Geometric surface area calculated (Zeo++)	283.27 m^2 g^{-1}
BET surface area from experimental N_2 isotherm /77 K	982.97 m^2 g^{-1}
Pore volume calculated (Zeo++)	0.11 cm^3 g^{-1}
Pore volume from experimental N_2 isotherm /77 K	0.41 cm^3 g^{-1}
the largest cavity diameter (LCD) calculated(Zeo++)	10.28 Å

Supplementary Table 4. Langmuir-Freundlich parameter fits for C_2H_2, C_2H_4, and C_2H_6 in Azole-Th-1.

	q_{sat} mol kg^{-1}	b_0 Pa$^{-\nu}$	E kJ mol^{-1}	ν dimensionless
C_2H_2	11.0	2.260E-8	19.2	0.79
C_2H_4	6.8	4.932E-10	24.8	1.00
C_2H_6	6.2	7.649E-12	32.0	1.18

Supplementary Table 5. Energies of single models and respective complexes and the binding energies for the models bonded C_2H_6/C_2H_4

	E_{MOF} (Hartree)	$E_{\text{MOF-C2H6}}$ (Hartree)	$E_{\text{MOF-C2H4}}$ (Hartree)	$\Delta E_{\text{bind}}(C_2H_6)$ (kJ mol^{-1})	$\Delta E_{\text{bind}}(C_2H_4)$ (kJ mol^{-1})
M1	-3443.372	-3523.109	-3521.870	-25.87	-13.33
M2	-3443.374	-3523.119	-3521.885	-46.90	-46.06
M3	-3443.377	-3523.121	-3521.886	-42.91	-41.69
M4	-3443.375	-3523.124	-3521.881	-56.69	-33.01
Average				-43.09	-33.52

Supplementary Table 6. The number of vdW interactions between C-H of C_2H_6/C_2H_4 with different regions in models

	M1		M2		M3		M4		**All (C_2H_6)**	**All (C_2H_4)**
	C_2H_6	C_2H_4	C_2H_6	C_2H_4	C_2H_6	C_2H_4	C_2H_6	C_2H_4		
I region	4(3.70)	4(3.30)	4(3.63)	2(3.55)	4(3.73)	4(3.45)	4(3.60)	3(3.33)	**16(3.67)**	**13(3.41)**
II region	0	0	4(3.50)	3(3.50)	2(3.35)	0	2(4.10)	1(3.00)	**8(3.65)**	**4(3.25)**
III region	2(2.95)	0	0	0	1(3.20)	0	0	0	**3(3.08)**	**0**
All	**6(3.45)**	**4(3.30)**	**8(3.57)**	**5(3.52)**	**7(3.43)**	**4(3.45)**	**6(3.77)**	**4(3.33)**		

Noted: the distances of interaction also listed in the brackets, the unit is Å.

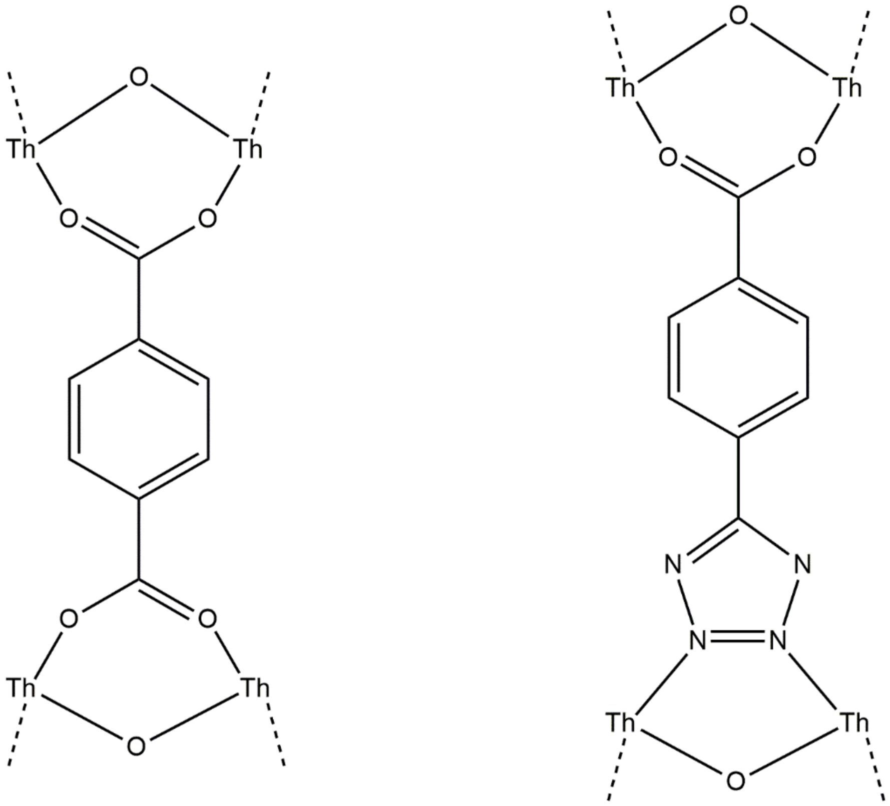

Typical mode of Zr$_6$ or Th$_6$ based MOFs **Mixed mode of Th$_6$ based MOFs**

Supplementary Figure 1. Two coordination modes. The modes of Zr(IV) or Th(IV) based MOFs using the carboxylic acid ligand (typical coordination mode) and azole ligand (mixed coordination mode), respectively.

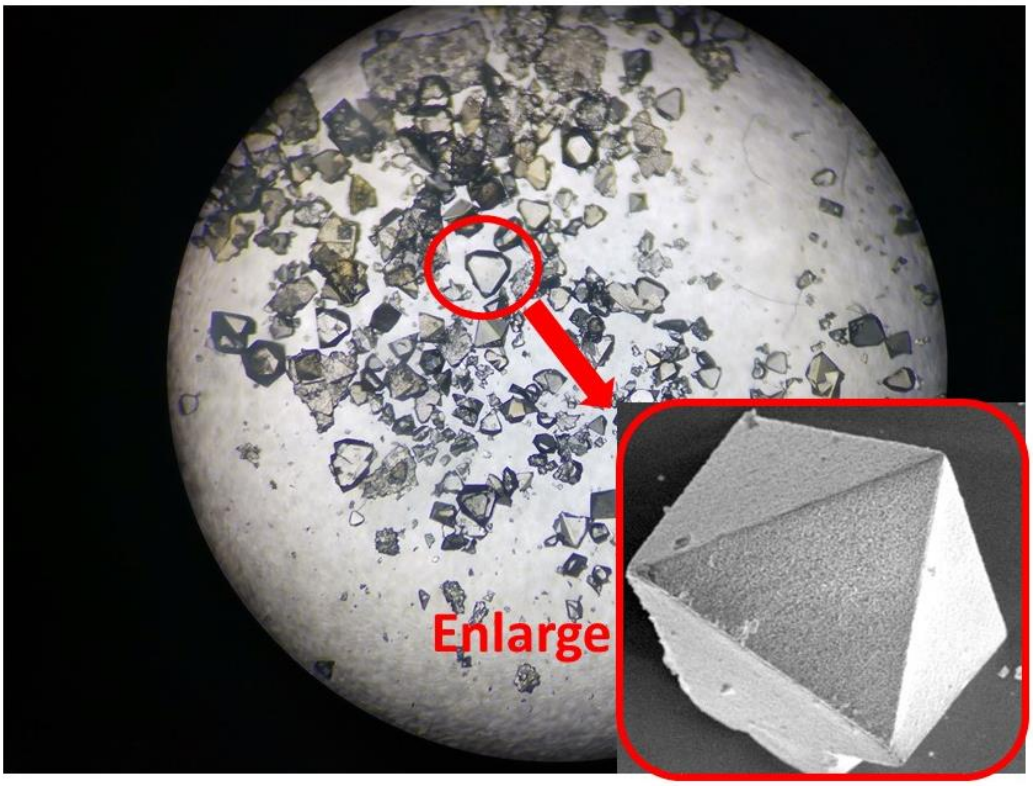

Supplementary Figure 2. Enlarged drawing of optical microscope images of Azole-Th-1 samples. The obvious octahedral crystal was obtained.

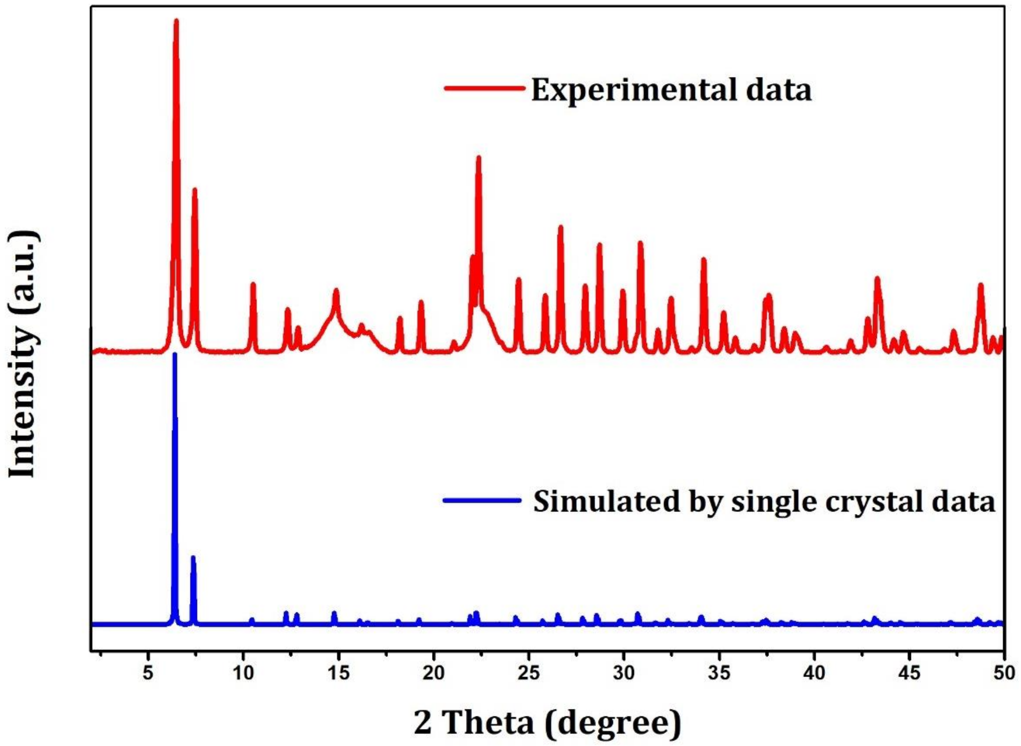

Supplementary Figure 3. **The PXRD patterns of Azole-Th-1 sample.** The experimental results of as-synthesized samples and the simulation from single crystal. Source data are provided as a Source Data file.

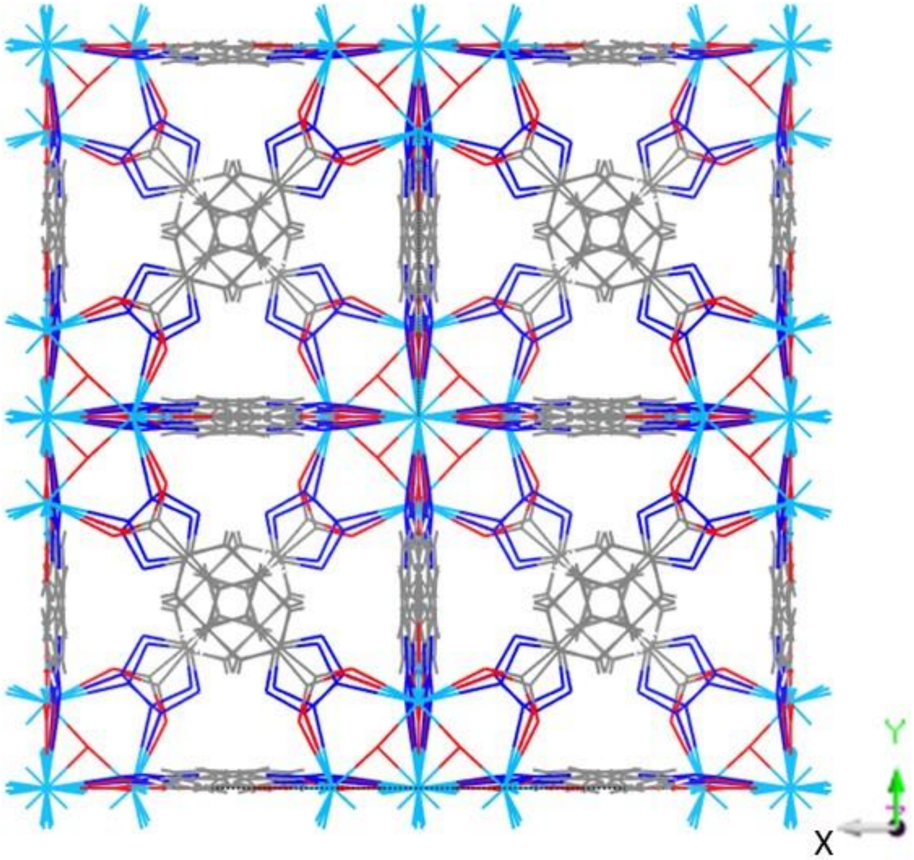

Supplementary Figure 4. **The crystal structure of Azole-Th-1 by the disordered ligand TBA**.

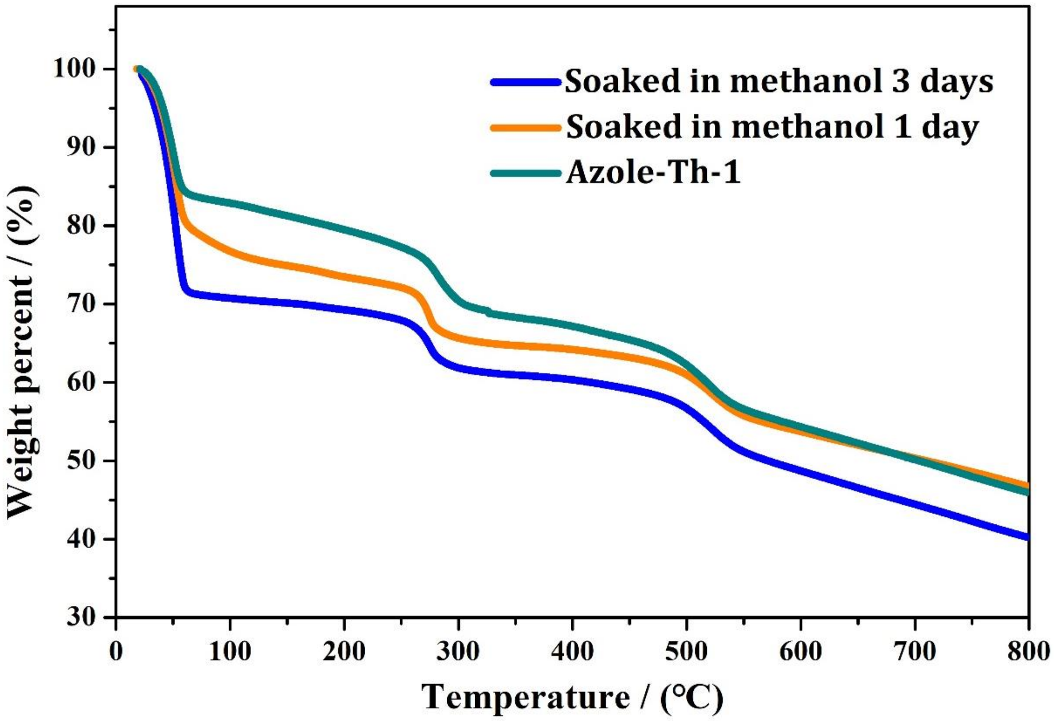

Supplementary Figure 5. The TG analysis. The as-synthesized Azole-Th-1 samples, and the samples soaked in methanol for three days and one day under N_2 atmosphere by 2°C per min of ramp rate. The loss of major trapped solvent DMF from Azole-Th-1 sample is before 75℃, the plateau region is descending slightly due to the incomplete loss of DMF molecules. And then, the plateau region is still not obvious for sample soaked in methanol one day, which indicates that the solvent exchange is still incomplete. After the sample soaked in methanol three days, the clear plateau region appears, the solvent exchange is complete. Source data are provided as a Source Data file.

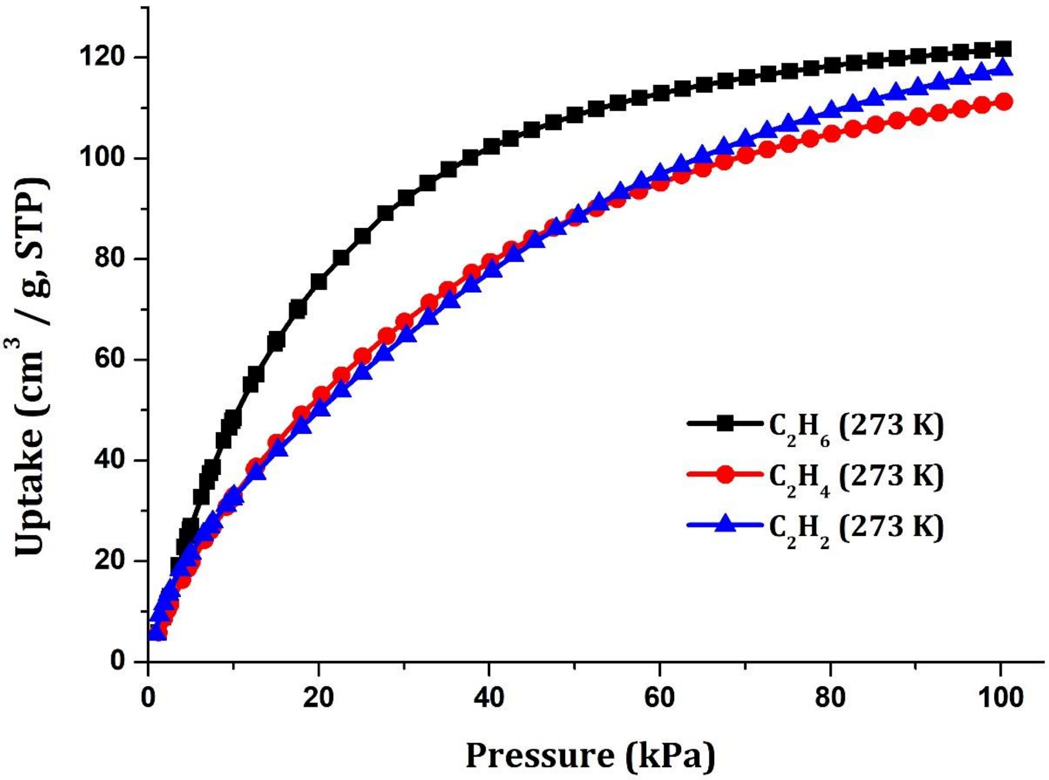

Supplementary Figure 6. The adsorption isotherms of Azole-Th-1. The experimental adsorption isotherms of Azole-Th-1 for C_2H_6, C_2H_4 and C_2H_2 at 273 K from 0.001 to 100 kPa. Source data are provided as a Source Data file.

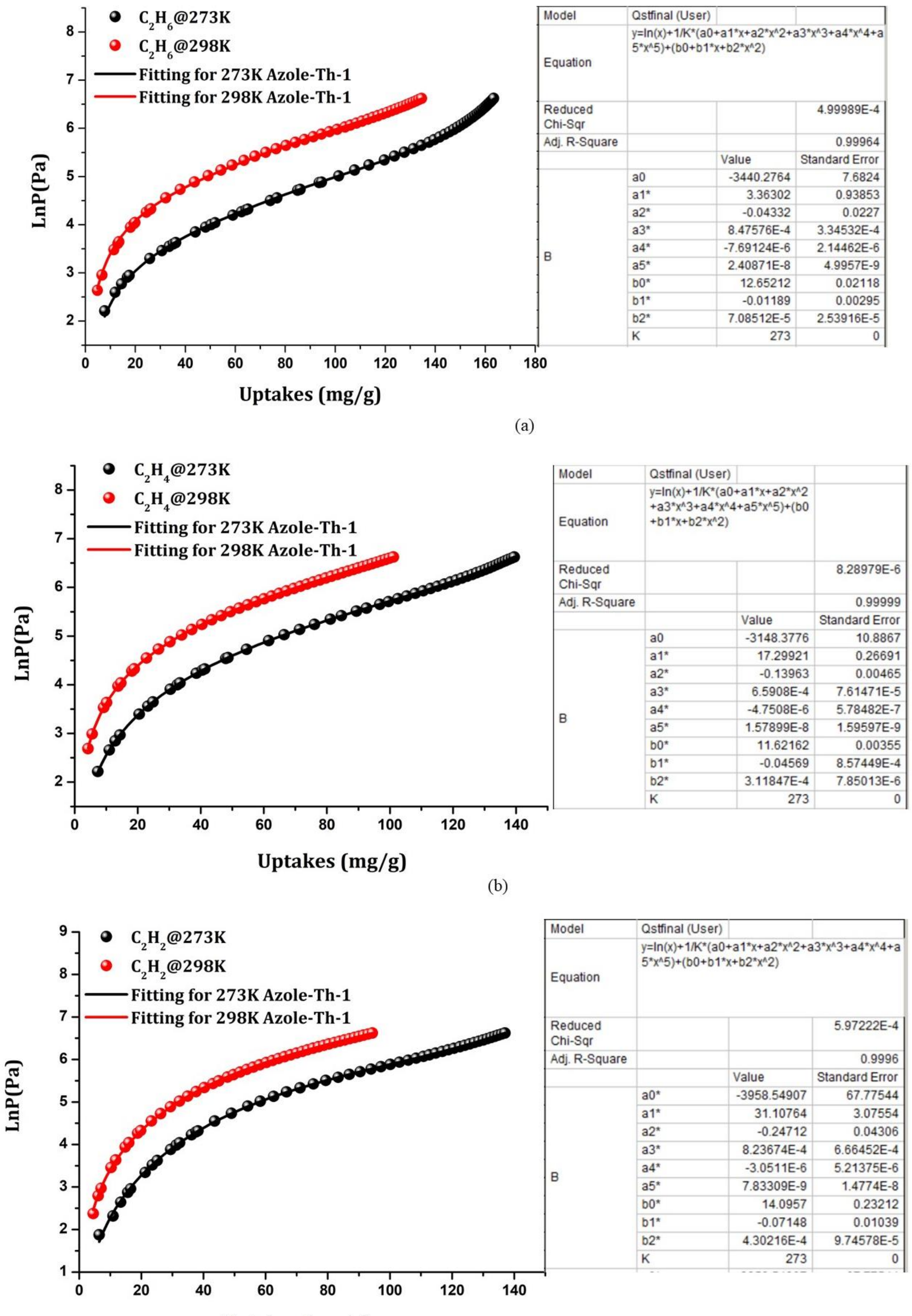

Model	Qstfinal (User)		
Equation	y=ln(x)+1/K*(a0+a1*x+a2*x^2+a3*x^3+a4*x^4+a5*x^5)+(b0+b1*x+b2*x^2)		
Reduced Chi-Sqr			4.99989E-4
Adj. R-Square			0.99964
		Value	Standard Error
B	a0	-3440.2764	7.6824
	a1*	3.36302	0.93853
	a2*	-0.04332	0.0227
	a3*	8.47576E-4	3.34532E-4
	a4*	-7.69124E-6	2.14462E-6
	a5*	2.40871E-8	4.9957E-9
	b0*	12.65212	0.02118
	b1*	-0.01189	0.00295
	b2*	7.08512E-5	2.53916E-5
	K	273	0

(a)

Model	Qstfinal (User)		
Equation	y=ln(x)+1/K*(a0+a1*x+a2*x^2+a3*x^3+a4*x^4+a5*x^5)+(b0+b1*x+b2*x^2)		
Reduced Chi-Sqr			8.28979E-6
Adj. R-Square			0.99999
		Value	Standard Error
B	a0	-3148.3776	10.8867
	a1*	17.29921	0.26691
	a2*	-0.13963	0.00465
	a3*	6.5908E-4	7.61471E-5
	a4*	-4.7508E-6	5.78482E-7
	a5*	1.57899E-8	1.59597E-9
	b0*	11.62162	0.00355
	b1*	-0.04569	8.57449E-4
	b2*	3.11847E-4	7.85013E-6
	K	273	0

(b)

Model	Qstfinal (User)		
Equation	y=ln(x)+1/K*(a0+a1*x+a2*x^2+a3*x^3+a4*x^4+a5*x^5)+(b0+b1*x+b2*x^2)		
Reduced Chi-Sqr			5.97222E-4
Adj. R-Square			0.9996
		Value	Standard Error
B	a0*	-3958.54907	67.77544
	a1*	31.10764	3.07554
	a2*	-0.24712	0.04306
	a3*	8.23674E-4	6.66452E-4
	a4*	-3.0511E-6	5.21375E-6
	a5*	7.83309E-9	1.4774E-8
	b0*	14.0957	0.23212
	b1*	-0.07148	0.01039
	b2*	4.30216E-4	9.74578E-5
	K	273	0

(c)

Supplementary Figure 7. The virial equation fitting curves for adsorption isotherms of Azole-Th-1. (a) C_2H_6, (b) C_2H_4, and (c) C_2H_2.

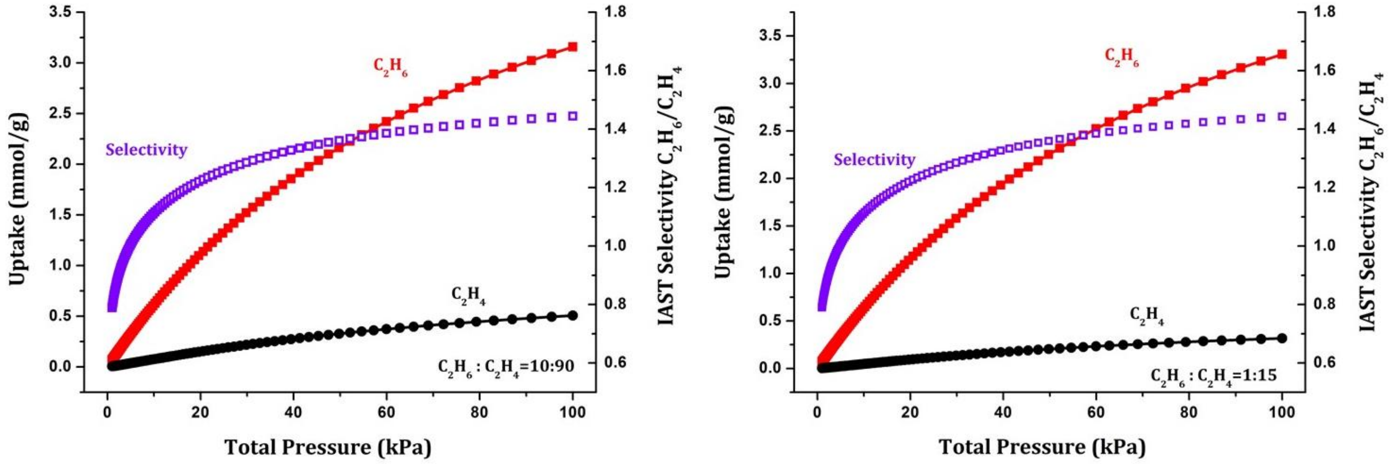

(a) (b)

Supplementary Figure 8. Predicted mixture adsorption isotherms and selectivity by IAST method. (a) 10/90 and (b) 1/15 C_2H_6/C_2H_4 mixture at 298 K . Source data are provided as a Source Data file.

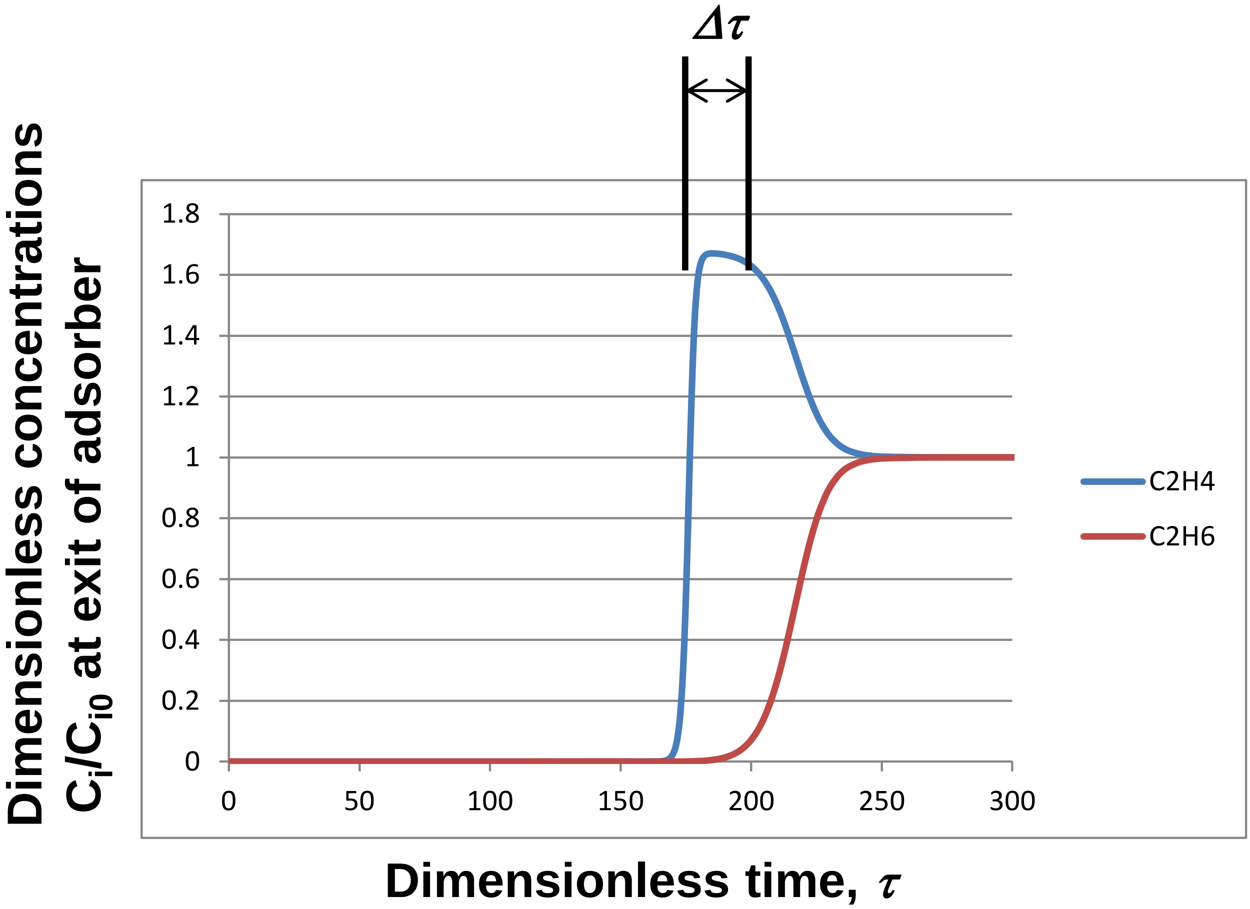

Supplementary Figure 9. The simulated transient breakthrough curve for Azole-Th-1. C_2H_6/C_2H_4 (50:50, v/v) binary mixture at 298 K and 1 bar. Source data are provided as a Source Data file.

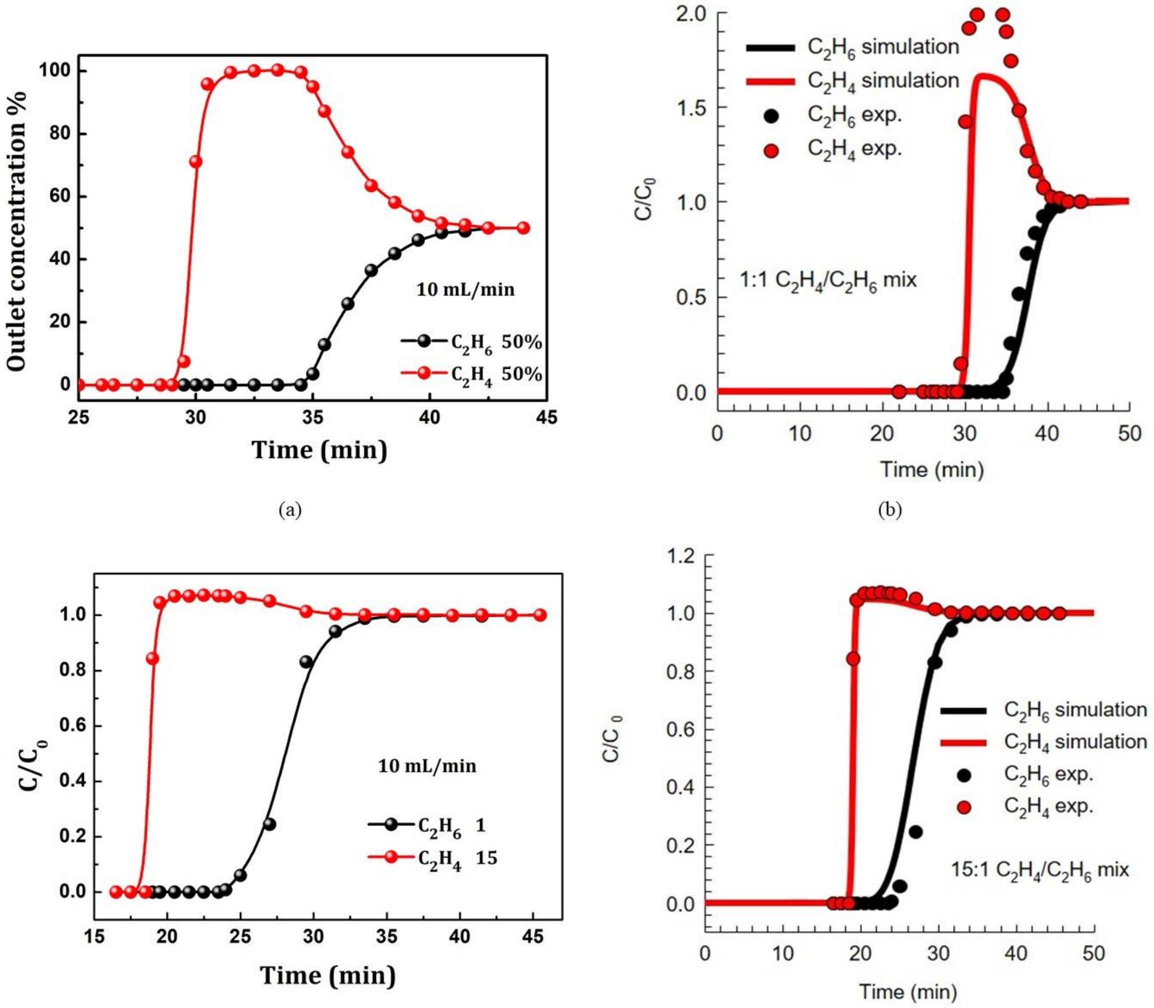

(a) (b)

(c) (d)

Supplementary Figure 10. The experimental breakthrough curves for Azole-Th-1 at 298 K and 1 bar. (a) and (b) C_2H_6/C_2H_4 (50/50, v/v) and (c) and (d) C_2H_6/C_2H_4 (1/15, v/v) binary mixture. Source data are provided as a Source Data file.

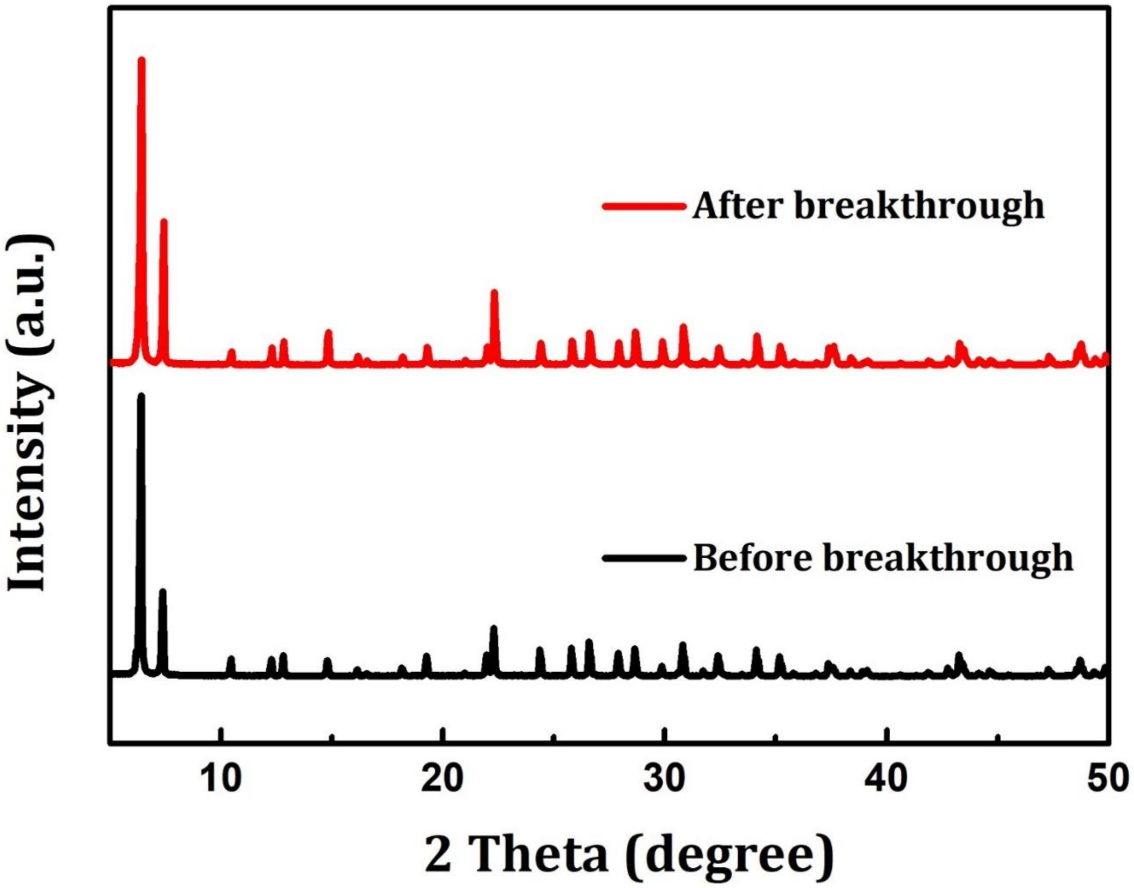

Supplementary Figure 11. The PXRD patterns of Azole-Th-1 samples. Before and after breakthrough experiments for binary mixture C_2H_6/C_2H_4. Source data are provided as a Source Data file.

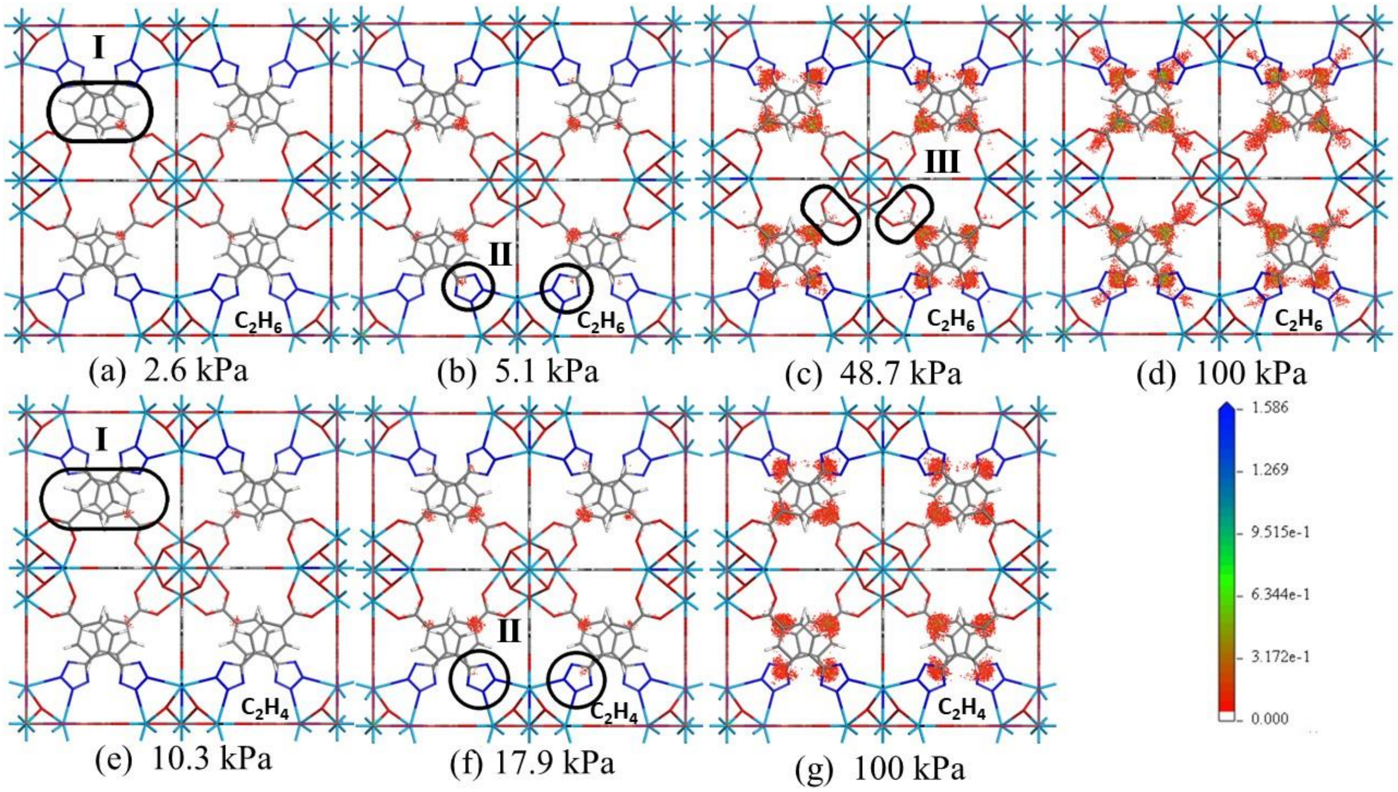

(a) 2.6 kPa (b) 5.1 kPa (c) 48.7 kPa (d) 100 kPa

(e) 10.3 kPa (f) 17.9 kPa (g) 100 kPa

Supplementary Figure 12. The density distribution of C_2H_6/C_2H_4 through GCMC simulations at 298 K. (a) 2.6 kPa, (b) 5.1 kPa, (c) 48.7 kPa, and (d) 100 kPa for C_2H_6, and (e) 10.3 kPa, (f) 17.9 kPa, and (g) 100 kPa for C_2H_4. Where, Th-light blue, O-red, C-grey, N-blue, and H-white, the 'color dots' denoted the size of density distribution according to the color bar.

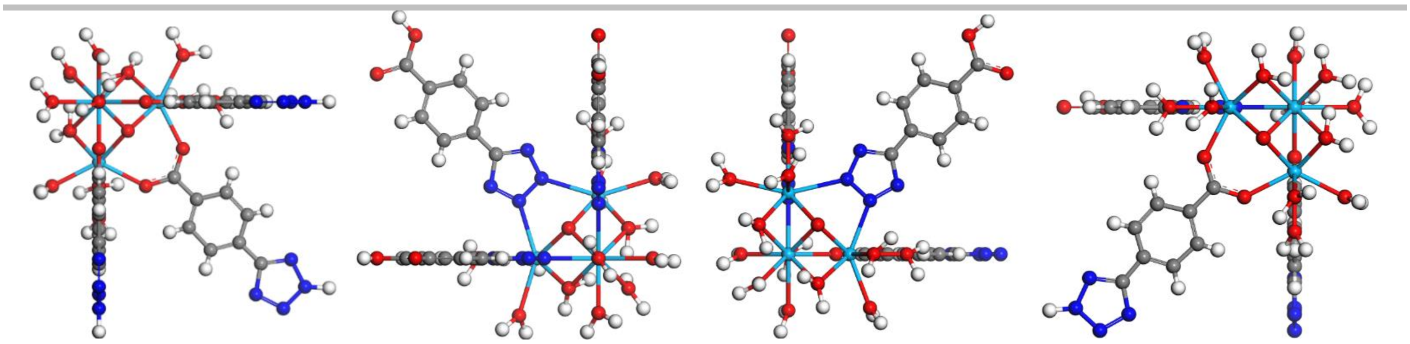

M1 M2 M3 M4

Supplementary Figure 13. The optimized four fragmented models M1 to M4. Where, Th-light blue, O-red, C-grey, N-blue, and H-white.

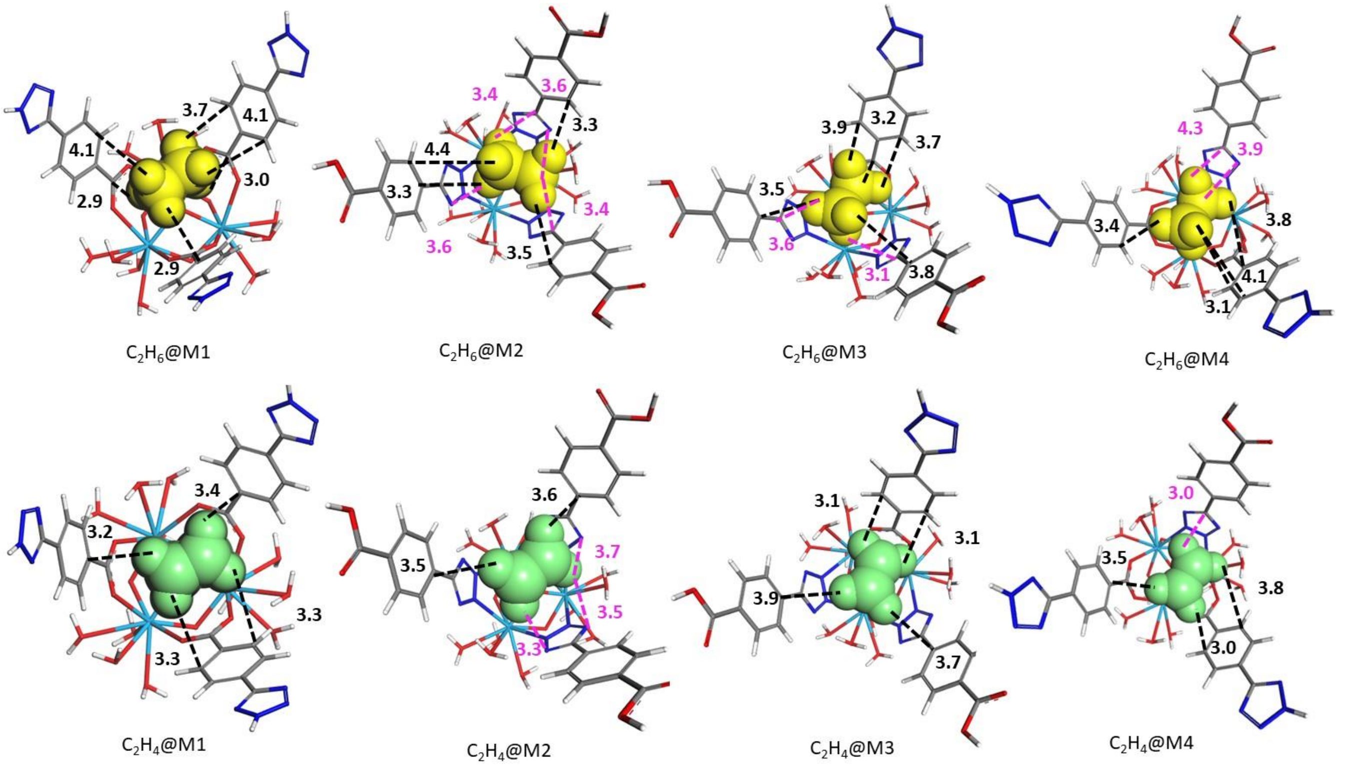

Supplementary Figure 14. The adsorbed structures for C_2H_6/C_2H_4@M1 to M4. Where, C_2H_6-yellow molecule, C_2H_4-green molecule, Th-light blue, O-red, C-grey, N-blue, and H-white, and the unit of distance is Å.

Supplementary References

1. Willems TF, Rycroft CH, Kazi M, Meza JC, Haranczyk M. Algorithms and tools for high-throughput geometry- based analysis of crystalline porous materials. *Microporous Mesoporous Mater* **149**, 134-141 (2012).

2. Martin RL, Smit B, Haranczyk M. Addressing challenges of identifying geometrically diverse sets of crystalline porous materials. *J Chem Inf Model* **522**, 308-318 (2012).

3. Material Studio.). Versiono 8.0 edn. Accelrys Inc. (2014).

4. Allen MP, Tildesley DJ. *Computer Simulation of Liquids*. Clarendon Press (1987).

5. Frenkel D, B S. *Understanding Molecular Simulation: From Algorithms to Applications*. Academic Press (2002).

6. Czepirski L, Jagiello J. Virial-type thermal equation of gas—solid adsorption. *Chem Eng Sci* **44**, 797-801 (1989).

7. Rowsell JLC, Yaghi OM. Effects of functionalization, catenation, and variation of the metal oxide and organic linking units on the low-pressure hydrogen adsorption properties of metal-organic frameworks. *J Am Chem Soc* **128**, 1304-1315 (2006).

8. Perdew JP, Burke K, Ernzerhof M. Generalized gradient approximation made simple. *Phys Rev Lett* **77**, 3865-3868 (1996).

9. Grimme S, Ehrkich S, Goerigk L. Effect of the damping function in dispersion corrected density functional theory. *J Comput Chem* **32**, 1456-1465 (2011).

10. Delley B. From molecules to solids with the Dmol^3 approach. *J Chem Phys* **113**, 7756 (2000).

11. Bezus AGK, A. V.; Lopatkin, A. A.; Pham, Q. D. . *J Chem Soc, Faraday Trans 2,* **74,** , 367 (1978).

12. Mayo SL, Olafson BD, III WAG. *J Phy Chem* **94**, 8897-8909 (1990).

13. Krishna R. The Maxwell-Stefan Description of Mixture Diffusion in Nanoporous Crystalline Materials. *Microporous Mesoporous Mater* **185**, 30-50 (2014).

14. Krishna R. Methodologies for Evaluation of Metal-Organic Frameworks in Separation Applications. *RSC Advances* **5**, 52269-52295 (2015).

15. Krishna R. Screening Metal-Organic Frameworks for Mixture Separations in Fixed-Bed Adsorbers using a Combined Selectivity/Capacity Metric. *RSC Advances* **7**, 35724-35737 (2017).

16. Krishna R. Methodologies for Screening and Selection of Crystalline Microporous Materials in Mixture Separations. *Sep Purif Technol* **194**, 281-300 (2018).

17. Krishna R, Baur RD. Adsorption and reaction in zeolites: Modelling and numerical issues. *http://krishnaamsterchemcom/zeolite/*, *University of Amsterdam, Amsterdam*, (1 January 2015).

18. Li L, *et al.* Ethane/ethylene separation in a metal-organic framework with iron peroxo sites. *Science* **362**, 443-446 (2018).

19. Liao PQ, Zhang WX, Zhang JP, Chen XM. Efficient purification of ethene by an ethane-trapping metal-organic framework. *Nat Commun* **6**, 8697 (2015).

20. Pires Jo, Pinto MsL, Saini VK. Ethane selective IRMOF-8 and its significance in ethane−ethylene separation by adsorption. *ACS Appl Mater Interfaces* **6**, 12093−12099 (2014).

21. Wu Y, Chen H, Liu D, Qian Y, Xia H. Adsorption and separation of ethane/ethylene on ZIFs with various topologies: Combining GCMC simulation with the ideal adsorbed solution theory (IAST). *Chem Eng Sci* **124**, 144-153 (2015).

22. Chen D, Wang N, Xu C, Tu G, Zhu W, Krishna R. A combined theoretical and experimental analysis on transient breakthroughs of C_2H_6/C_2H_4 in fixed beds packed with ZIF-7. *Microporous Mesoporous Mater* **208**, 55-65 (2015).

23. Gücüyener C, van den Bergh J, Gascon J, Kapteijn F. Ethane/ethene separation turned on its head: selective ethane adsorption on the metal-organic framework ZIF-7 through a gate-opening mechanism. *J Am Chem Soc* **132**, 17704-17706 (2010).

24. Van den Bergh J, Gucuyener C, Pidko EA, Hensen EJ, Gascon J, Kapteijn F. Understanding the anomalous alkane selectivity of ZIF-7 in the separation of light alkane/alkene mixtures. *Chem Eur J* **17**, 8832–8840 (2011).

25. Chen Y*, et al.* An ethane-trapping MOF PCN-250 for highly selective adsorption of ethane over ethylene. *Chem Eng Sci* **175**, 110-117 (2018).

26. Liang W*, et al.* Ethane selective adsorbent Ni(bdc)(ted)$_{0.5}$ with high uptake and its significance in adsorption separation of ethane and ethylene. *Chem Eng Sci* **148**, 275-281 (2016).

27. Qazvini OT, Babarao R, Shi ZL, Zhang YB, Telfer SG. A robust ethane-trapping metal-organic framework with a high capacity for ethylene purification. *J Am Chem Soc* **141**, 5014-5020 (2019).

28. Lv D*, et al.* Selective adsorption of ethane over ethylene in PCN-245: Impacts of interpenetrated adsorbent. *ACS App Mater Interfaces* **10**, 8366-8373 (2018).

29. Chen Y*, et al.* Highly adsorptive separation of ethane/ethylene by an ethane-selective MOF MIL-142A. *Ind Eng Chem Res* **57**, 4063-4069 (2018).

30. Lin RB*, et al.* Boosting ethane/ethylene separation within isoreticular ultramicroporous metal-organic frameworks. *J Am Chem Soc* **140**, 12940-12946 (2018).

31. Chen K-J*, et al.* Synergistic sorbent separation for one-step ethylene purification from a four-component mixture. *Science* **366**, 241-246 (2019).